Nonlinear dynamics of new magneto-mechanical oscillator

Zhifeng Hao[a,b,*], Dan Wang[a,b,c], Marian Wiercigroch[b,*]

[a] *School of Mathematical Sciences, University of Jinan, Jinan 250022, China*
[b] *Centre for Applied Dynamics Research, School of Engineering, University of Aberdeen, Aberdeen, AB24 3UE Scotland, UK*
[c] *Nanjing University of Aeronautics and Astronautics, Nanjing 210016, China*

Abstract

This study presents modelling and analysis of a new magneto-mechanical (MM) oscillator (Nonlinear Dyn 99:323-339,2020), which pays a special attention to mechanical and magnetic nonlinearities for large amplitude responses. The oscillator is comprised of a box structure made of two parallel leaf springs with one end fixed and the other clamped with a proof mass, and an electromagnetic actuator. A solenoid and a permanent magnet are the main parts of the actuator, which acts directly on the proof mass providing an accurate and versatile excitation by varying intensity and frequency of the input current. The new model for a beam of large deflection is based up the constitutive relation of nonlinear beam theory. A new design of the electromagnetic actuator with a pair of identical solenoids and a new concept of quasi-constant force (QCF) are proposed, which aim to generate a nearly constant force for a constant input current. The mathematical model of the MM oscillator is systematically developed and discussed for different types of excitations depending on designs and parameters of the electromagnetic actuator. The undertaken nonlinear dynamics analysis further demonstrates versatility of the electromagnetic actuator to generate a wide spectrum of excitations. The prediction from the modelling were validated with the experimental results from the previous work (Nonlinear Dyn 102:835-861,2020). The study demonstrates that the electromagnetic actuator provides versatile excitation patterns and can be used to study experimentally subtle nonlinear phenomena.

Keywords: Magneto-mechanical oscillator, Constitutive relation, Electromagnetic actuation, Nonlinear dynamics

1. Introduction

Modelling and analysis of nonlinear oscillators play a vital role in our understanding, application and controlling of various types of vibration in mechanical systems and structures. The analysis methodologies of nonlinear oscillators provide valuable theoretical and applied insight if the modelling

*Corresponding author
Email addresses: zhifenghao@hotmail.com (Zhifeng Hao), danwang2014518@hotmail.com (Dan Wang), m.wiercigroch@abdn.ac.uk (Marian Wiercigroch)

of the main nonlinear effects have been undertaken with care. Classical and new examples such as pendula [1–3], Duffing [4–7], Lorenz [8–10], SD [11–13] and impact [14–18] oscillators, demonstrate diverse forms of nonlinear oscillations. In recent years, lots of nonlinear mechanical oscillators have been developed due to the application-driven theoretical and experimental studies. Several comprehensive reviews can serve as guides how to utilize various of nonlinear oscillators for vibration isolation [19–25], vibration absorption [26–29] and energy harvesting [30–36], and for other applications.

A large variety of beam structures are used as stiffness elements in above-mentioned applications and theoretical studies, for instance, cantilever beams, buckled beams, nanobeams, as well as beams with different shapes and configurations, which have been extensively studies, e.g. see [37–48]. In 1980's, some scholars started to study the nonlinear dynamics of beam, e.g., Moon and Shaw *et al.* [49, 50], who reduced a cantilever beam by a Galerkin approximation to the Duffing oscillator. In this work, they focused on the study of twin-well dynamics and found strange attractors, and on the chaotic vibrations of a beam with an impact boundary condition. Recently, Ding *et al.* [51, 52], Yan *et al.* [53] and Wang *et al.* [54, 55] modelled a continuous fluid-conveying pipe as an Euler-Bernoulli beam, investigating the bending vibration modes and nonlinear responses also using the Galerkin method and the finite difference method. The elliptic integral approach is another classical method to solve the large nonlinear deformation of a slender structure in form of a beam or column, which accurately describes effects of loads on deflections [56, 57]. Batista [58] presented an exact analytical solution for the equilibrium configurations of a cantilever beam subjected to an inclined force and tip moment acting on its free end. By using this method, Virgin *et al.* [59] investigated the buckled characteristic of a simple beam subjected to an axial load. Emans *et al.* [60] considered the cumulative effect of nonlinearities of the beam and derived out an analytical third order expansions. Different from the above-mentioned methods, the first objective of this paper is to develop a lump parameter mathematical model of the beam structure composed of parallel leaf springs to accurately describe its geometry for large deflection.

The second objective of this work is to develop a comprehensive, accurate and computationally viable model of the electromagnetic force generation. In the recent years there has been a lot of investigations in this area and we will summarise the main developments. To develop an oscillating motor, a solenoid activated system with a RLC series circuit and a metal bar was designed by Nguyen *et al.* [61, 62], which was used to generate resonant vibro-impacts. Xu *et al.* [63] modelled an electro-magnetic shaker as two and a half degrees-of-freedom system, and studied the dynamics of the pendulum-shaker system theoretically and experimentally. A capsule system was proposed to explore vibro-impact responses to realize self-propelled locomotion by Liu *et al.* [64–66], where a DC step motor and gear mechanism were used to generate excitations. In [67], the authors explored magnets and excitation coils to drive an inverted pendulum of piezoelectric energy harvester, aimed

at developing micro and nanomechanical resonators. Wang *et al.* [68] presented electromagnetic quasi-zero-stiffness resonators periodically to realize the semi-active metamaterial beam. A cantilever beam-based electromagnetic resonator with electromagnetic and mechanical damping was investigated in [69]. Piezoelectric type actuator is other type which has been often used for vibration control of beams [70]. Moreover, a nonlinear electromagnetic shunt damping for vibration isolators has been investigated in [71–73], where a pair of the permanent magnets and a pair of the coils are applied to produce electromagnetic damping force mechanisms. Liu et al. [74] employed a magnetic interaction to improve the performance of a multi-direction vibration isolator theoretically and experimentally. Witkowski *et al.* in [75] used a pair of permanent magnets to serve as magnetic springs and studied the dynamics of two degrees-of-freedom mechanical system. From this brief review, it is apparent that a simple and reliable actuator design is of great interest both fundamentally and practically to provide arbitrarily desired types of excitations as a vibration source, a vibration controller and an electromagnetic damper. To authors knowledge, a design of versatile, robust and accurate actuator still presents a significant challenge [76, 77].

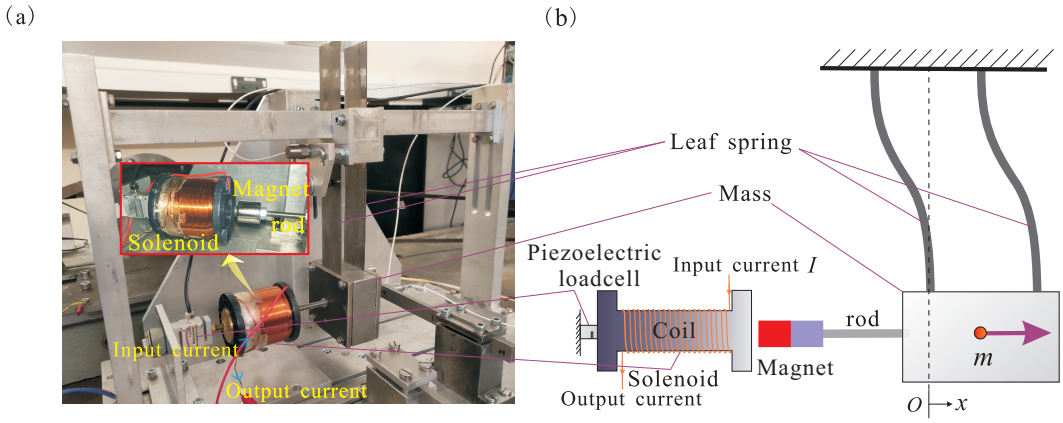

Figure 1: (colour online) New magneto-mechanical oscillator: (a) a phototype of the experimental setup [78], (b) a schematic diagram of the oscillator. The main components of the system are a coil, a permanent magnet, a steel linked rod, a proof mass, and a pair of adjustable length of leaf springs as well as sensors (the eddy current probe and accelerators to record the motion of beam and the support platform, a piezoelectric load cell as a force transducer to evaluate the reaction force resulting from the interactions of the magnetic field of the solenoid with the magnet). The current is provided by a control system with a Proportional Integral Derivative (PID) controller program created in Labview, which can supply a required current in the coil. The current signal from Labview needs to be amplified using the DC power supplier.

Recently, a new magneto-mechanical (MM) oscillator has been designed and studied by the Centre for Applied Dynamics Research at the University of Aberdeen (see Figure 1), which has been early applied to study subtle bifurcation scenarios in a soft impacting oscillator [78–80]. For small amplitudes of vibration, the experimental study indicated the stiffness of the two parallel leaf springs structure was linear and the electromagnetic force was harmonic. For large oscillations the system is strongly

nonlinear due to the large deflection of structure and electromagnetic force generation mechanisms. To this end, several new ideas are presented here in order to design a versatile and robust electromagnetic actuator, which can provide a wide range and highly controllable excitations pattern including harmonic ones where the frequency and amplitude can be adjusted independently. Additionally, from the view point of dynamics, stability and bifurcations will be investigated comprehensively by advanced nonlinear dynamics analysis methods.

This paper is structured as follows. In Section 2, a new analysis method is presented to model the large-deflection beam structure of parallel leaf springs based up the constitutive relation from nonlinear beam theory. In Section 3, we derive the mathematical model of electromagnetic actuator by applying the infinitesimal element analysis method and the charge model. This section will study the nature of actuating force and then propose a new quasi-constant force actuator for a versatile exciter, for which an optimization will be carried out to broaden the nearly constant force range. In Section 4, the dynamic model of the MM oscillator is derived and dynamics and bifurcation analysis are conducted for harmonic, parametric and harmonic-parametric electromagnetic force. The availability of the new proposed twin-solenoid electromagnetic actuator to supply various types of excitations is demonstrated in this section. In Section 5, experimental studies are implemented to validate the theoretical model. In Section 6, concluding remarks are drawn.

2. Mathematical model of large-deflection beam

In this section, a new computation approach is presented to solve the large deflection problems of beam with a shape under the first order vibration mode. The new proposed method to obtain the lumped parameter model of the oscillator is based upon the constitutive relation of nonlinear beam theory. By analyzing the data derived from the constitutive equations, the polynomial fit based upon the least square method will be implemented in the second subsection to obtain the relationship between the displacement and restoring force.

2.1. Constitutive relations

The bending problem of a parallel leaf spring beam is schematically presented in Figure 2, which is similar to other beam structures such as cantilever and clamped-clamped ones. Additionally, it should be pointed out that the two leaf springs shown in Figure 1 are identical with the same constraints, so the problem can be simplified into deflection of one spring.

Under the assumption that the material of beam remains linearly elastic, the relationship of bending moment and beam deformation reads

$$\kappa = \frac{\mathrm{d}\theta}{\mathrm{ds}} = \frac{M(s)}{EI} = \frac{\omega''}{\left(1+\omega'^2\right)^{\frac{3}{2}}}, \tag{1}$$

where κ is the curvature of the beam deflection curve, θ, s, $M(s)$, ω are the tangent angle from the x-axis, the curvilinear coordinate, the bending moment and the transverse displacement of the considered infinitesimal beam element, respectively, and EI is the bending stiffness of the beam, as well as the prime denotes the derivative with regards to x. Additionally, see Eq. (A.1) describing the relationship between ω and θ.

As shown in Figure 2 depicting an infinitesimal element of the beam, the relationship between the bending moment $M(s)$ and the internal shear force Q can be derived out (see A.2 and A.3 for more details) as the following

$$Q = \frac{\mathrm{d}M}{\mathrm{d}s} = \frac{\mathrm{d}M}{\mathrm{d}x} \cdot \frac{\mathrm{d}x}{\mathrm{d}s} = \left[EI \frac{\omega''}{(1+\omega'^2)^{\frac{3}{2}}} \right]' \cdot \cos\theta = -P\cos\theta + G\sin\theta, \tag{2}$$

where the force P acted on the mass M and the gravity G of the mass are considered and the mass of the leaf springs are neglected herein.

According to Eq. (2) and letting $\phi = \omega'$, the following equation can be obtained

$$\phi'' - \frac{3\phi}{1+\phi^2}\phi'^2 = -\frac{P}{EI}(1+\phi^2)^{\frac{3}{2}} + \frac{G}{EI}\phi(1+\phi^2)^{\frac{3}{2}}. \tag{3}$$

In addition, the parallel spring leaf beam should satisfy the following boundary conditions $\omega(0) = 0, \omega'(0) = 0, \omega'(l) = 0, s(0) = 0, s(l) = L$. Combining Eqs (1) and (3), the exact mathematical model of the studied beam will be established and reduced into first order differential equations with boundary constraint conditions as follows

$$\begin{cases} \omega' = \tan\theta = \phi, \\ \phi' = u, \\ u' = \frac{3\phi u^2}{1+\phi^2} - \frac{P}{EI}(1+\phi^2)^{\frac{3}{2}} + \frac{G}{EI}\phi(1+\phi^2)^{\frac{3}{2}}, \\ s' = \sqrt{1+\phi^2}, \\ \omega(0) = 0, \phi(0) = 0, \phi(l) = 0, s(0) = 0, s(l) = L. \end{cases} \tag{4}$$

There are four differential equations and five boundaries conditions. Taking account into one of the two boundary conditions for the curvilinear coordinate s as $s(0) = 0$, the solution of the system can be found by adjusting parameter l to satisfy $s(l) = L$. This is the first boundary value problem of high order ordinary differential equations, which can be computed by using the routine bvp4/5/6c in Matlab [81]. From Eq. (4), the vibration characteristics of the beam with the mass subjected to point loads can be easily obtained. Example curves are given in Figure 3, which are obtained for parameters listed in Table 1.

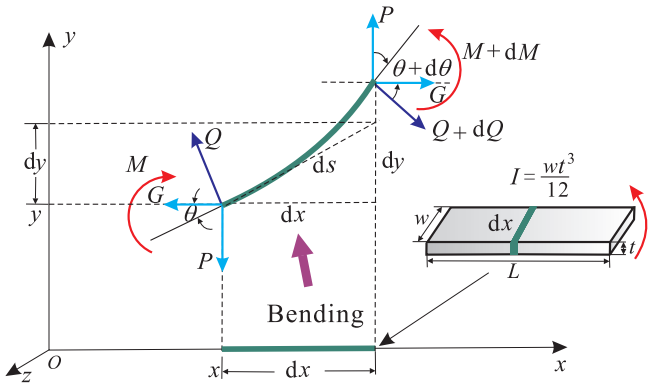

Figure 2: (colour online) Free-body diagrams of an element of the beam, where M, Q, P and G denote the bending moment, the internal shear force, the force acting on the mass and the gravity of the mass, and dx, dy, ds express the differentials of the beam element in x and y directions and the arc differential, respectively.

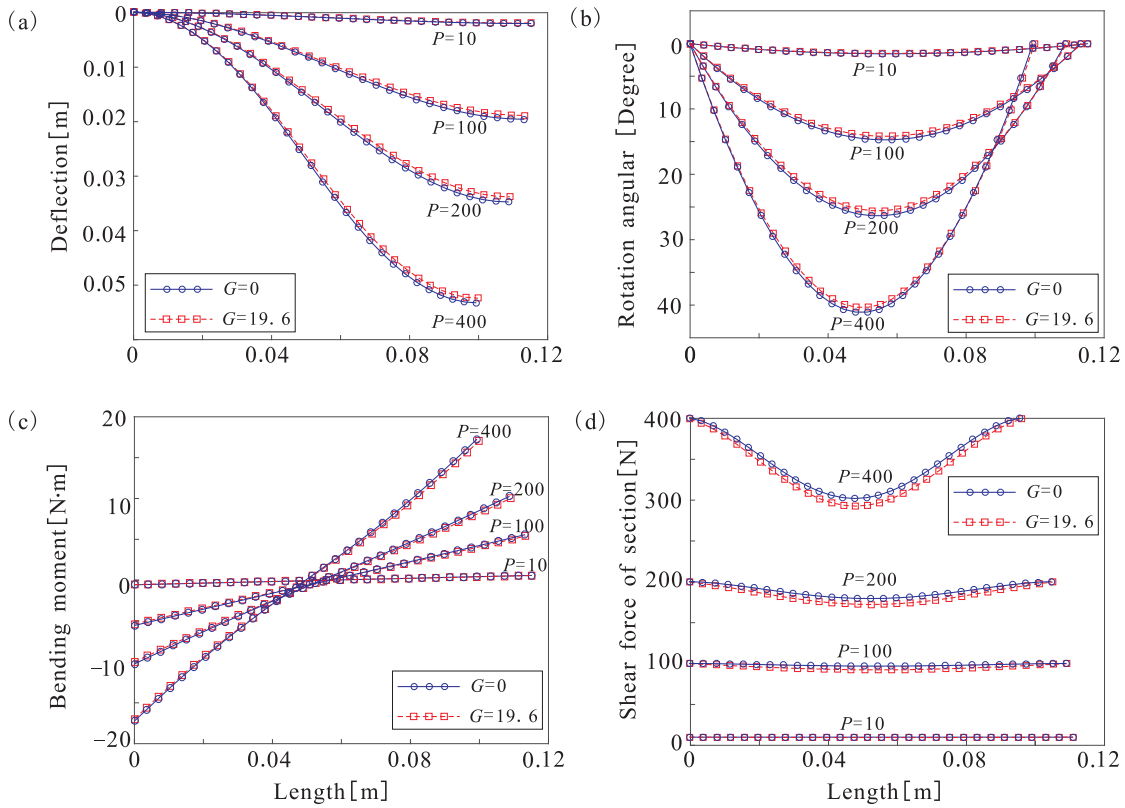

Figure 3: (colour online) The response characteristics of the beam of parallel leaf springs when the tip mass is loaded by the static force P (P=10 N, 100 N, 200 N, 400 N marked in each panel): (a) the deflection, (b) the rotation angular, (c) the bending moment, (d) the shear force in the beam cross-section. The red square-dashed lines and the blue circle-solid lines show the cases of with and without gravity influences considered, respectively.

Table 1: Geometric and material properties of the oscillator.

Parameter (symbol)	Value	Parameter (symbol)	Value
Width(w)	0.035 m	Length (L)	0.115 m
Thickness (t)	0.001 m	Force (P)	0-500 N
Young's modulus (E)	210 GPa	Gravity of tip mass (G)	19.6 N

2.2. Restoring force analysis

For a simple harmonic oscillator, the restoring force is a force acting opposite to displacement to bring the system back to an equilibrium. The force magnitude depends only on displacement obeying Hookes law $F_s = -kx$, where F_s is the restoring force and k is the stiffness. The restoring force of a large-deflection beam can be defined similarly, which is equal to the force required to make the beam deviate from its equilibrium position but in the opposite direction. The stiffness will be defined as the derivative of the restoring force with respect to the deflection amount. Figure 4 computed based on the values from Table 1, shows the relationships between the acting force and displacement x, where the blue dotted line and the red dotted line represent the required force without a tip mass considered and with a tip mass of gravity 19.6 N considered, respectively. It can be seen clearly that the restoring force is nonlinear with respect to displacement for large deflections, and the gravity of tip mass reduces the restoring force in the motion direction for the same deflection, and it makes a hard nonlinearity of the beam structure even stronger. Meanwhile, it is shown that the contribution of the gravity is weak in small deflections, and becomes strong as the deflection becomes large. In addition, the acting force was computed by two formula (see Appendix A.2 and [46, 60] for details) and marked with the black dot-dot-dashed line and the green solid line in Figure 4, respectively. A comparison of above results indicates that the mathematical model corresponds well to the literatures and can describe the restoring force well only for small beam deflections.

In order to describe a relationship between the force and the displacement, a polynomial fit based upon the least square method can be applied of the form shown below

$$F_n(x) = a_n x^n + a_{n-1} x^{n-1} + \ldots + a_1 x + a_0,$$

where the restoring force $F_n(x)$ is connected with the displacement x and a_i is the coefficient of the polynomial with respect to the term of the i-th power of x. The mathematical approach for finding the best-fitting polynomial curve of a given set of points by minimizing the sum of the squares of the offsets of the points from the curve, for which the well-established routines can be used [82, 83]. It is important to evaluate the goodness of the fitting curve, which can be done by computing the residual

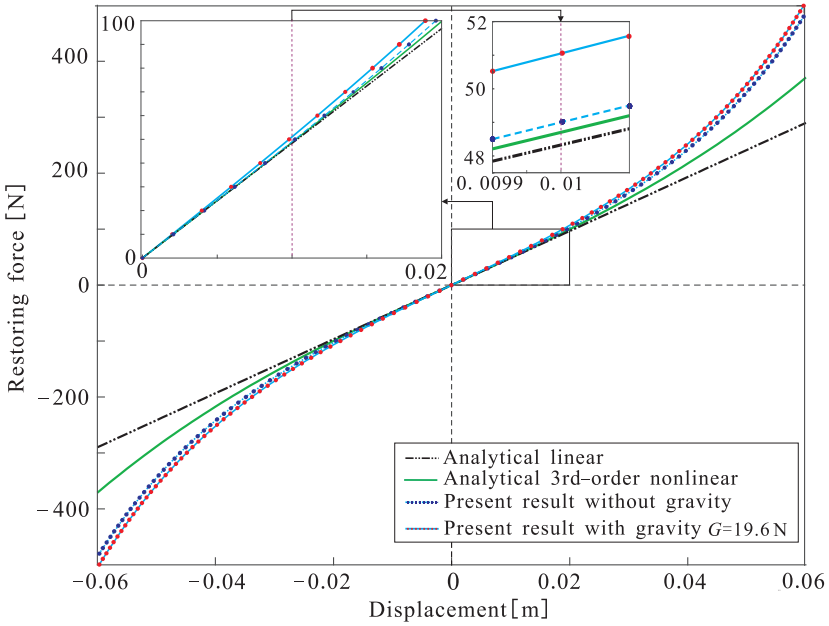

Figure 4: (colour online) Restoring forces: linear and cubic nonlinear analytical curves introduced in Appendix A.2, and the exact results derived from Equation (4) for the cases of with gravity and without gravity.

norm (RN)

$$\mathrm{RN} = \sqrt{\sum_{i=1}^{n} (\hat{y}_i - y_i)^2}, \tag{5}$$

where $\hat{y}_i$ is the fitting data corresponding to x_i. Table 2 lists the fitting coefficients of the restoring forces versus the deflections for the data from Eq. (4) with a maximum deflection of 10 mm, which compares the two cases of with and without gravity considered. Figure 5(a) shows the raw data of the restoring forces versus deflections within the maximum deflection of 60 mm, where the gravity is considered. Meanwhile, the fitting curves F_3, F_5, F_7 are plotted, whose coefficients are listed in Table 3. Furthermore, the residual errors of the raw data minus the fitting data are presented in Figure 5(b), which indicates the seventh order fit is the best.

Table 2: Fitting polynomials and related residual norms

F_n (Without gravity)	$a_3(\times 10^5)$	$a_1(\times 10^3)$	RN	F_n (With gravity)	$a_3(\times 10^5)$	$a_1(\times 10^3)$	RN
F_1	0	4.8758	0.3694	F_1	0	5.0780	0.3348
F_3	6.68783	4.8329	0.0077	F_3	6.80021	5.0376	0.0049

Table 3: Fitting polynomials and related residual norms

F_n	$a_7(\times 10^{10})$	$a_5(\times 10^7)$	$a_3(\times 10^5)$	$a_1(\times 10^3)$	RN
F_3	0	0	11.18785	4.6065	40.7870
F_5	0	14.262998	5.33044	5.0991	3.9040
F_7	1.57705897	5.0654423	6.87475	5.0328	0.5565

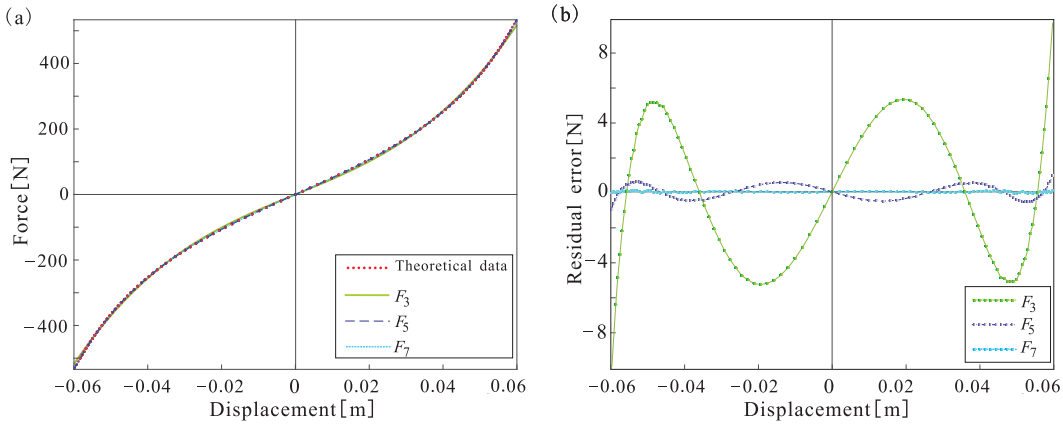

Figure 5: (colour online) (a) Comparisons between the exact force and the polynomial fitting results for the third-order, fifth-order and seventh-order models, that is, F_3, F_5, F_7, with coefficients listed in Table 3. (b) Residual errors of the fitting curves versus the exact force.

3. Mathematical model of electromagnetic actuator

In this study, the magneto-mechanical oscillator is driven by a cylindrical permanent magnet plunger, which is acted upon by an external magnetic field generated by a solenoid as shown in Figure 6(a). Using the Biot-Savart law and the differential element method, the magnetic field at any point along the axial direction of the coils can be modelled. The force acting on the cylindrical magnet bar in the external magnetic field can be calculated based upon the charge model introduced in [84]. It should be noted that if the cylindrical magnet moves along the axis of the coil, there will be no lateral force due to symmetry. However in our experimental rig, in case of a large deflection the frame structure induces small vertical motion. Therefore, the axial amplitude of oscillations in all our experimental studies has been limited to 10 mm. The horizontal lateral forced was balanced out by positioning the magnet symmetrically in the coil. Hence, by taking these precautions the influence of lateral forces can be neglected. Additionally, an improved design of the electromagnetic actuator with a pair of identical solenoids is developed and discussed in this section, which aims at generating a constant force for a constant current.

3.1. Modelling of electromagnetic forces

To calculate the magnetic flux density B at the arbitrary point P along the axis of the solenoid, an infinitesimal element from a loop of the coil marked by $\mathrm{d}\vec{l}$ in Figure 6(b) is considered. According

to the Biot-Savart law, the magnetic flux density at desired point P can be written as a vector form as it follows

$$\mathrm{d}\vec{B} = \frac{\mu_0 I}{4\pi}\frac{\mathrm{d}\vec{l}\times\vec{r}}{r^3} = \frac{\mu_0 I}{4\pi}\frac{\mathrm{d}\vec{l}\times(\vec{r}_p-\vec{r}')}{r^3} = \frac{\mu_0 I}{4\pi}\frac{R\mathrm{d}\theta\vec{\mathrm{e}}_{\vec{\theta}}\times(x\vec{i}-R\vec{\mathrm{e}}_{\vec{r}'})}{|x\vec{i}-R\vec{\mathrm{e}}_{\vec{r}'}|^3}, \tag{6}$$

where I is the current passing through the coils, μ_0 is the vacuum permeability that is a constant $4\pi\times10^{-7}$H/m, R is the radius of the coils, $\vec{\mathrm{e}}_{\vec{\theta}}$, $\vec{\mathrm{e}}_{\vec{r}'}$ and $\vec{i}$ are the unit vectors in directions of $\vec{\theta}$, $\vec{r}'$ and x-axis, respectively. Consequently,

$$\mathrm{d}\vec{B}=\frac{\mu_0 IxR}{4\pi(x^2+R^2)^{\frac{3}{2}}}\mathrm{d}\theta\vec{\mathrm{e}}_{\vec{r}'}+\frac{\mu_0 IR^2}{4\pi(x^2+R^2)^{\frac{3}{2}}}\mathrm{d}\theta\vec{i}. \tag{7}$$

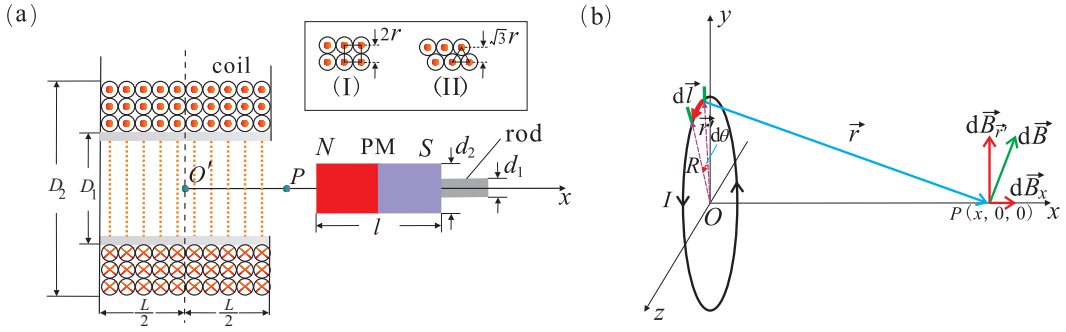

Figure 6: (colour online) (a) A schematic of the single solenoid actuator (sectional view: the orange dashed lines express the coil wire, and the dot-circles and cross-circles show the current entering and leaving the cross section of the wire), which is comprised of a coil and a magnet cylinder linking with a steel rod. (b) The magnetic flux of an infinitesimal element in a loop of the current coil: $\mathrm{d}\vec{B}$ denotes the magnetic flux at an arbitrary point P in x-axis, while $\mathrm{d}\vec{B}_x, \mathrm{d}\vec{B}_{\vec{r}'}$ represent its axial and radial components, respectively. The box shows two potential configurations of winding wires, (I) and (II).

Considering the magnetic field at point P generated by the single current coil shown in Figure 6(b), the magnetic flux in the plane that is parallel to $\vec{r}'$ is zero, because integrating the unit vector of $\vec{r}'$ along an entire loop of the coils equals zero. Hence, only the magnetic field in the x-axis direction needs to be considered, that is,

$$\vec{B}_x = \int_0^{2\pi}\frac{\mu_0 IR^2}{[x^2+R^2]^{\frac{3}{2}}}\mathrm{d}\theta\,\vec{i} = \frac{\mu_0 IR^2}{2(x^2+R^2)^{\frac{3}{2}}}\vec{i}. \tag{8}$$

Taking into account a cross-section along the radius direction of the solenoid, the number of turns of coils through a unit area is

$$n = \frac{N}{(\frac{D_2}{2}-\frac{D_1}{2})L} = \frac{2N}{(D_2-D_1)L},$$

so the current differential element passing through the unit area is

$$\mathrm{d}I = I(n\mathrm{d}x\mathrm{d}R) = nI\mathrm{d}x\mathrm{d}R. \tag{9}$$

By substituting Eq. (9) into Eq. (8), a variation of the magnetic field at an arbitrary point P along $x-$axis is described as

$$\mathrm{d}B_x = \frac{\mu_0 R^2}{2(x^2+R^2)^{\frac{3}{2}}}\mathrm{d}I = \frac{\mu_0 NIR^2}{(D_2-D_1)L(x^2+R^2)^{\frac{3}{2}}}\mathrm{d}x\mathrm{d}R. \tag{10}$$

Integrating Eq. (10) over the above-mentioned cross-section, the magnetic flux at point P is obtained

$$\begin{aligned} B_x &= \frac{\mu_0 NI}{(D_2-D_1)\cdot L}\int_{\frac{D_1}{2}}^{\frac{D_2}{2}}\int_{-\frac{L}{2}}^{\frac{L}{2}}\frac{\tilde{R}^2}{[(x-\tilde{x})^2+\tilde{R}^2]^{\frac{3}{2}}}\mathrm{d}\tilde{x}\mathrm{d}\tilde{R} \\ &= \frac{\mu_0 NI}{2(D_2-D_1)\cdot L}\left[(L-2x)\ln\frac{D_2+\sqrt{(2x-L)^2+D_2^2}}{D_1+\sqrt{(2x-L)^2+D_1^2}} + (L+2x)\ln\frac{D_2+\sqrt{(2x+L)^2+D_2^2}}{D_1+\sqrt{(2x+L)^2+D_1^2}}\right]. \end{aligned} \tag{11}$$

Based upon the charge model introduced in [84], the force of the permanent in an external magnet field can be expressed by

$$\vec{F} = \int_V \rho\vec{B}_{ext}\mathrm{d}v + \oint_s \sigma\vec{B}_{ext}\mathrm{d}s, \tag{12}$$

where $\vec{B}_{ext}$ is the external magnetic field, $\vec{M}$ is the magnetic moment per unit volume of the permanent magnet, $\rho = -\nabla\cdot\vec{M}$ and $\sigma = \vec{M}\cdot\vec{n}$ are equivalent volume and surface charge density, respectively. Additionally, the magnetic moment can be obtained by the equation $\vec{M} = B_r/\mu_0$, where B_r is the residual flux density of the permanent magnet. Note that the cylinder magnetic plunger is polarized along its axis with fixed and uniform magnetization written as $\vec{M} = M_s\vec{i}$, hence $\rho = -\nabla\cdot\vec{M} = 0$ and the magnetic force along the $x-$axis is

$$F_x = \oint_s \sigma B_x\mathrm{d}s. \tag{13}$$

Let us consider that the magnetic plunger is a hollow cylinder. To evaluate σ, we firstly determine the unit surface normals as

$$\vec{n} = \begin{cases} -\vec{i}, & x_l = x - \frac{l}{2}, \\ \vec{i}, & x_r = x + \frac{l}{2}, \\ -\vec{\mathrm{e}}_{\vec{r}}, & r = \frac{d_1}{2}, \\ \vec{\mathrm{e}}_{\vec{r}}, & r = \frac{d_2}{2}, \end{cases}$$

where x_l and x_r are the coordinate of the left and right area of the permanent magnet in $x-$axis, and l, d_1, d_2 are the length, the outer and inner radius of the magnet cylinder, respectively. It should be pointed out that the centre of the solenoid is selected as the coordinate origin of the $x-$axis herein.

Because $\vec{e}_{\vec{r}} \perp \vec{M}$, it is known that $\sigma = 0$ in the cylindrical surface of the magnet plunger. Suppose that the left and right hand sides of the permanent magnet are the north and south poles respectively, and the charge density in the end surface of the permanent magnet is described as

$$\sigma = \begin{cases} M, & x_l = x - \frac{l}{2}, \\ -M, & x_r = x + \frac{l}{2}. \end{cases} \tag{14}$$

Applying Eqs (12) and (14), the force on the permanent magnet plunger is derived as

$$\begin{aligned} F_x &= \oint_s \sigma_m B_x \mathrm{d}s = M\left[B_x(x-\tfrac{l}{2}) - B_x(x+\tfrac{l}{2})\right] \int_{\frac{d_1}{2}}^{\frac{d_2}{2}} \int_0^{2\pi} r \mathrm{d}r\mathrm{d}\phi \\ &= \tfrac{B_r \pi (d_2^2 - d_1^2)}{4\mu_0} \left[B_x(x-\tfrac{l}{2}) - B_x(x+\tfrac{l}{2})\right], \end{aligned} \tag{15}$$

where $B_x(\cdot)$ is the function with respect to the variable x. The magnetic force generated by the actuator is shown in Figure 7, which is plotted by using the parameter values listed in Table 5 and B_r taken as 1.28 T herein. This figure also indicates that the maximum actuation force is produced when the centre of the magnet moves close to the coil end for a single solenoid actuator.

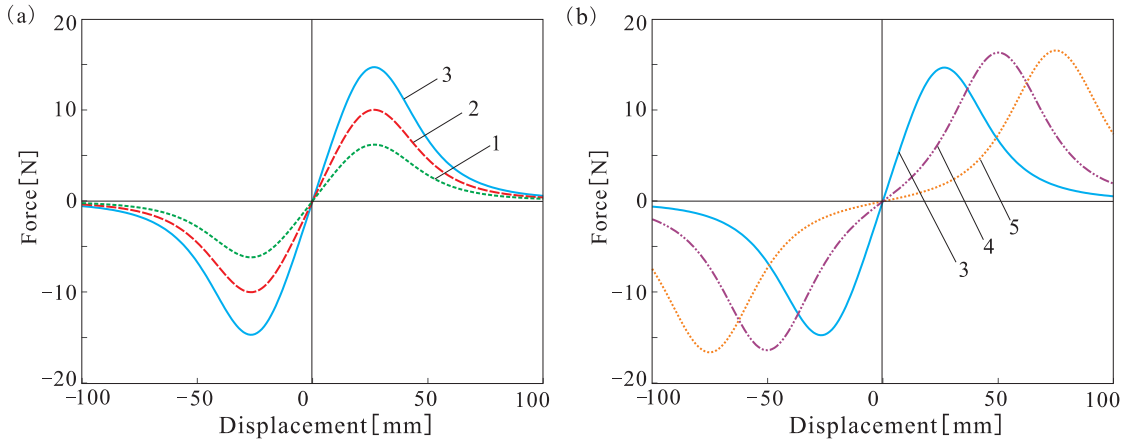

Figure 7: (colour online) The force characteristic of the single solenoid actuator for different parameters listed in Table 5: (a) d_2 is set as 0.020 m, 0.025 m, 0.030 m, while other parameters keep unchanged, (b) L is taken as 0.05 m, 0.10 m, 0.15 m, while other parameters are the same.

Table 4: Parameters of the electromagnetic actuator (see Figure 6 for details).

Parameters of solenoid	Symbols	Parameters of magnetic plunger	Symbols
Current	I	Residual flux density	B_r
Turns of coil	N	Inner diameter	d_1
Inner diameter	D_1	Outer diameter	d_2
Outer diameter	D_2	Length	l
Length	L		

Figures 8(a) and 8(b) show ten electromagnetic force curves generated by the single solenoid

Table 5: Parameters for Figure 7 to show the characteristics of solenoid actuation forces.

Line numbers	Parameters							
	D_1(m)	D_2(m)	N	I(A)	$L(m)$	d_1(m)	d_2(m)	l(m)
1	0.05	0.06	540	5	0.05	0.006	0.020	0.02
2	0.05	0.06	540	5	0.05	0.006	0.025	0.02
3	0.05	0.06	540	5	0.05	0.006	0.030	0.02
4	0.05	0.06	1080	5	0.10	0.006	0.030	0.02
5	0.05	0.06	1620	5	0.15	0.006	0.030	0.02

actuator with parameters D_1=0.10 m, D_2=0.20 m, L=0.15 m, d_1=0.006 m, d_2=0.03 m, l=0.03 m and with constant current intensities between 1 A and 10 A. Figure 8(b) demonstrates that there is almost a linear relationship between the generated force and the magnet location in the solenoid. Hence, the actuation force can also be modelled by a polynomial expression as follows

$$F_m(x,t) = F_0 + \sum_{i=1}^{n} G_i x^i. \tag{16}$$

To explore the dynamic responses of the oscillator driven by the excitation shown in Figure 8, we take a typical region enlarged in its panel (b) as an interesting example and model the force curve as a linear model for the constant current $I = I_0$, that is,

$$F_m(x,t) = F_0 + G_1 x,$$

which corresponds to a harmonic-parametric excitation generated by the harmonic alternating current $I = I_0\cos(\Omega t)$, that is,

$$F_m(x,t) = (F_0 + G_1 x)\cos\omega t, \tag{17}$$

where the component of amplitude of force, $G_1 x$, is in relation to the displacement x of the magnet. In particular, when the magnet is placed in the centre of the solenoid, F_0 is equal to zero and the electromagnetic force becomes a typical parametric excitation.

3.2. An improved design of the electromagnetic actuator

From the above analysis for the single solenoid actuator, it is notable that the amplitude of driving force is dependent of displacement variance x. To generate a constant force that is independent of the displacement for the purpose of mechanical experiment, an improved electromagnetic actuator is proposed with a pair of identical and coaxial solenoids, where the coils are wound in the opposite directions and passed through the same currents. See details in Figure 9.

Assume the distance of centres (O' and O'') of the two solenoids is d, and choose the middle point of the axial line $O'O''$ is a coordinate origin O of the new system. In addition, it should be pointed

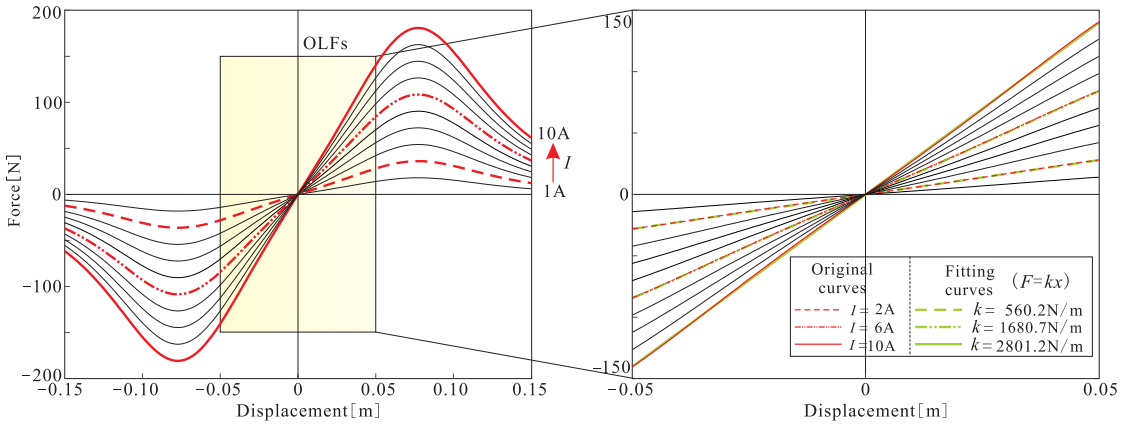

Figure 8: (colour online) Electromagnetic forces of a single solenoid actuator with $D_1 = 0.10$ m, $D_2 = 0.20$ m, $L = 0.15$ m, $d_1 = 0.006$ m, $d_2 = 0.03$ m, $l = 0.03$ m and the magnitudes of current increasing from 1 A to 10 A by one ampere.

out that the center of the magnetic plunger is located at the origin O along the axial line. By applying the Eq. (15), it can be derived that the electromagnetic force is

$$F = F_x(x - d/2) + F_x(x + d/2), \tag{18}$$

where $F_x(\cdot)$ is the function in regard to the variable x.

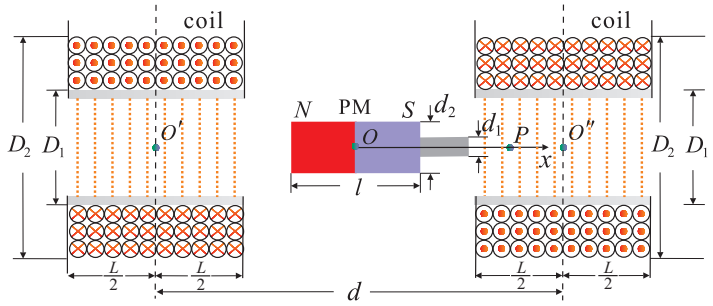

Figure 9: (colour online) Schematic of the twin-solenoids actuator (sectional view), where the magnet is placed at the centre between two identical solenoids. The pair of solenoids are of the same uniformly-wound coils passing the same current but with an opposite flow direction.

To examine the nature of the magnetic force for the new design, the parameters corresponding to Line 1 of Table 5 are used to construct the corresponding force curves, which are plotted in Figure 10. By analysing the characteristics of electromagnetic force generated by a constant direct current like those shown in Figure 10, the force can be classified into one of four types including quasi-constant force (QCF), oblique linear force (OLF), single peak force (SPF) and double peak force (DPF). It is worth pointing out that the new concept of the quasi-constant force is inspired by our earlier research on the quasi-zero stiffness vibration isolation [20, 85]. The different types of force reflect the

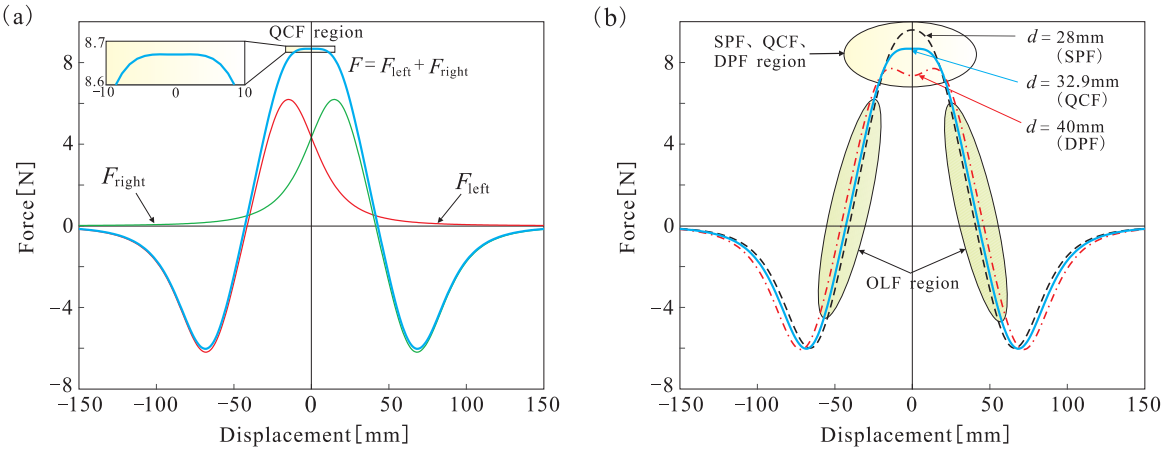

Figure 10: (colour online) (a) The quasi-constant force mechanism of the actuator of a pair of identical solenoids. (b) The force characteristic of the actuator by adjusting the distance between the pair of solenoids, where four types of force regions are shown, namely, the the quasi-constant force (QCF), the single peak force (SPF), the double peak force (DPF) and the oblique linear force (OLF).

dependencies between force and displacement, which can be obtained by adjusting the parameters of electromagnetic actuator, such as the length, thickness and radius of the solenoid, the number of turns of the coil, and the distance between a pair of solenoids. Figure 10(b) shows that there is the QCF zone around $x = 0$ when d=32.9 mm, and the force curves will become SPFs and DPFs as d gets bigger and smaller, for examples d=28 mm and d=40 mm, respectively. Similarly, the segments of OLF and SPF can be seen in Figure 7 for the single solenoid actuator. It should be pointed out that the single solenoid actuator can only generate OLFs and SPFs, and the actuator driven by a pair of identical solenoids can provide the four force types.

3.3. Optimization of quasi-constant force regions

In this section, optimization is carried out aiming at maximizing a quasi-constant force range shown in Figure 11, for which the selected parameters of the actuator of a pair of identical solenoids are listed in Table 6 and to obtain a 5 N quasi-constant force. Figure 11(a) shows the quasi-constant force region becomes wide as the length of the solenoid L increases with other parameters fixed. Similarly, Figures 11(b) and 11(c) present that increasing the parameters D_1, D_2, that is the inner and outer diameters of the solenoid, can also widen the range of the quasi-constant force. However, Figure 11(d) indicates changing the parameters of the magnet such as its length l herein has little influence on the quasi-constant force region. It is worth to note that for selected parameters of the solenoids and the magnet, the quasi-constant force can be obtained by adjusting the parameter d, namely the distance between the pair of solenoids. Importantly, a wide range of closely constant force can be obtained by fine tuning d to turn the quasi-constant force into a weak double peak force, which is demonstrated in Figures 11(e) and (f). Figure 11(f) is the enlargement of the small box in Figure

11(e) showing that the electromagnetic force at d=0.2394 m is a quasi-constant force depicted by the line 10, while the curve becomes a double peak force and a single peak force if d is increased and decreased, respectively. Two examples are depicted for d=0.2394 m and d=0.2200 m by the line 11 and the line 12 in Figure 11(f). It should be pointed out that selecting d=0.2394 m aims at obtaining a nearly constant force of 5 N with a wide effective range whilst with a small variance of magnitude of force. In this example, both of the deviation values from the maximum and minimum in the force curve 11 to the desired target force, namely 5 N, are 0.027 N, which has only a relative error of 0.54%. Consequently, the study indicates that L, D_1, D_2 are three dominant parameters to extend QCF regions, whilst fine tuning parameter d can also help to obtain a nearly constant force with an effectively wide range. The other parameters has a little influence on the range of quasi-constant force. Generally, according to the desired target force, the sizes of a magnet and the gauge of the coils should be selected in the first instance, and then an optimization procedure can implemented to obtain a family of optimized parameters.

Table 6: (colour online) Parameters for optimization studies in Figure 11, where the groups of compared parameters are colourfully marked (D_1 in red, D_2 in purple, L in green, d in blue, and l in pink) and the other parameters keep unchanged.

Line numbers	Parameters								
	D_1(m)	D_2(m)	N	I(A)	$L(m)$	d(m)	d_1(m)	d_2(m)	l(m)
1	0.20	0.22	1080	3.20171	0.05	0.1457	0.006	0.03	0.030
2	0.20	0.22	1080	1.88308	0.10	0.1243	0.006	0.03	0.030
3	0.20	0.22	1080	1.53718	0.15	0.11464	0.006	0.03	0.030
4	0.10	0.12	1080	1.06385	0.05	0.0699	0.006	0.03	0.030
5	0.15	0.17	1080	1.96777	0.05	0.1064	0.006	0.03	0.030
6	0.20	0.26	3240	1.24809	0.05	0.24809	0.006	0.03	0.030
7	0.20	0.30	5400	0.85848	0.05	0.1713	0.006	0.03	0.030
8	0.20	0.22	1080	4.74394	0.05	0.1437	0.006	0.03	0.020
9	0.20	0.22	1080	3.81624	0.05	0.1446	0.006	0.03	0.025
10	0.30	0.35	2700	2.91007	0.05	0.2394	0.006	0.03	0.030
11	0.30	0.35	2700	3.14655	0.05	0.2594	0.006	0.03	0.030
12	0.30	0.35	2700	2.69990	0.05	0.2200	0.006	0.03	0.030

4. Mathematical model and analysis of the magneto-mechanical (MM) oscillator

In this section, we develop the mathematical model of the MM oscillator and then test its dynamic responses. Initially dynamics of the oscillator will be studied to assess the versatility of the electromagnetic actuator in generating a wide spectrum of excitation. Then primary bifurcation scenarios of the oscillator under various patterns of excitation will be investigated by the direct numerical simulation and the harmonic balance method (HBM).

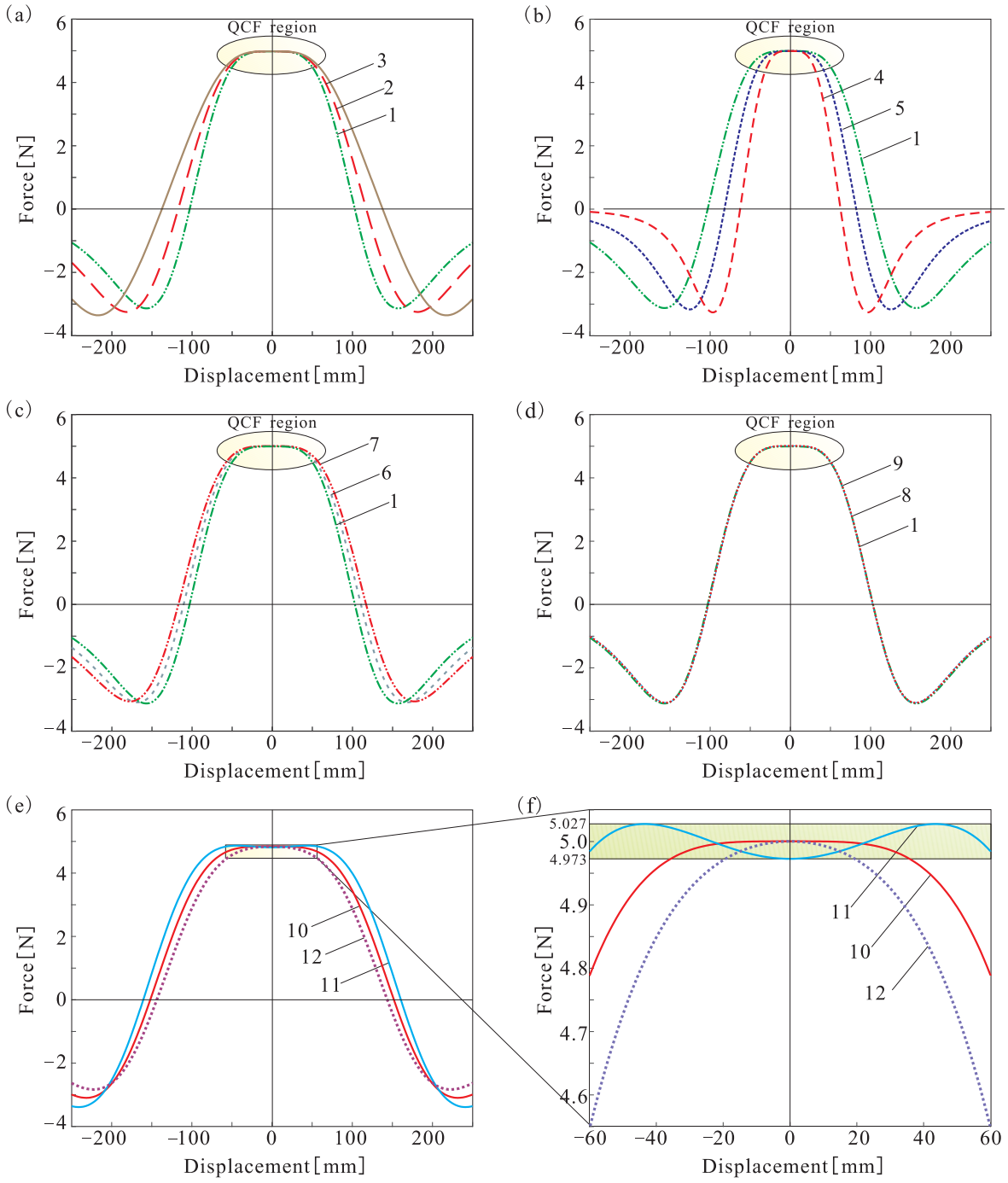

Figure 11: (colour online) Optimization to obtain wider regions of quasi-constant force, by analysing the parametric influence of the electromagnetic actuator system, such as parameters: (a-c) the length L, inner diameter D_1, outer diameter D_2 of the solenoid, (d) the length l of the permanent cylinder, (e) the distance between the centres of the twin-solenoids, (f) an enlargement of the small rectangular area from panel (e) to show the geometries of force curves as d varies.

4.1. Mathematical model and preliminary dynamic analysis of the MM oscillator

The MM oscillator is modelled as one degree-of-freedom nonlinear dynamical system driven by the electromagnetic force and its equation of motion for the magneto-mechanical oscillator can be expressed as

$$mx'' + F_{\mathrm{d}} + F_{\mathrm{b}}(x) = F_{\mathrm{m}}(t, x), \tag{19}$$

where m denotes the proof mass including the tip lumped mass and the mass of permanent magnet but neglecting the mass of leaf springs, $F_{\mathrm{d}} = C\dot{x}$ is the damping force, F_{b} and F_{m} are the restoring force of beam and the electromagnetic excitation. Based on the analysis undertaken in Section 2, we apply the restoring force model as a 7-*th* order polynomial, hence $F_{\mathrm{b}} = F_7$. For convenience of further analysis, Eq. (19) is nondimentionalised to the following form

$$\ddot{x} + 2\zeta\dot{x} + x + b_3x^3 + b_5x^5 + b_7x^7 = f_{\mathrm{m}}(\tau, x), \tag{20}$$

where $\omega_0 = \sqrt{a_1/m},\ \zeta = \frac{C}{2m\omega_0},\ \tau = \omega_0 t,\ b_3 = \frac{a_3}{m\omega_0^2},\ b_5 = \frac{a_5}{m\omega_0^2},\ b_7 = \frac{a_7}{m\omega_0^2},\ f_{\mathrm{m}}(x, \tau) = \frac{F_{\mathrm{m}}(x,t)}{m\omega_0^2}$.

The relation between the electromagnetic force and the location of the magnet in the solenoid and its influence on the oscillator behaviour are investigated. Figure 12 shows examples of restoring force characteristics (panel (a)), basins of attraction (panel (b)), as well as characteristics of electromagnetic (EM) driving force for various time histories (panel (c)).

Figure 12(a) depicts three electromagnetic force curves for the single solenoid actuator at three current intensities. In Figure 12(a), there are six points marked by the upper-roman letters from A to F, respectively, which are used to study the EM driving force characteristics for different magnet locations in the actuator. Figure 12(b) shows the basins of attraction and phase portraits of the MM oscillator driven by magnet at locations in the solenoid as those marked in Figure 12(a), where harmonic currents of intensity I_0 and frequency Ω=54 rad/s are used. It should be pointed out that the Poincaré map of the stroboscopic time $T = 2\pi/\Omega$ is constructed to implement the attraction basin analysis and to obtain the bifurcations diagrams (refer to [85] for more details). From the first three sub-figures of Figure 12(b), which have the same amplitude of excitation force of 5 N, it can clearly be seen that the basins of attraction and phase portraits are different, while the last three panels of Figure 12(b) further illustrate the effect of magnet locations on the dynamic responses. The column sub-figures of right-hand side in Figure 12(c) shows the characteristics of electromagnetic driving forces, which corresponds to time histories plotted in the left side sub-figures for cases from A to E. The driving force characteristics indicate that the single solenoid can be used as a harmonic exciter only in very small vibration amplitudes, such as in cases A and D for responses in blue, but no longer serving an ideal harmonic exciter for large amplitudes of vibration.

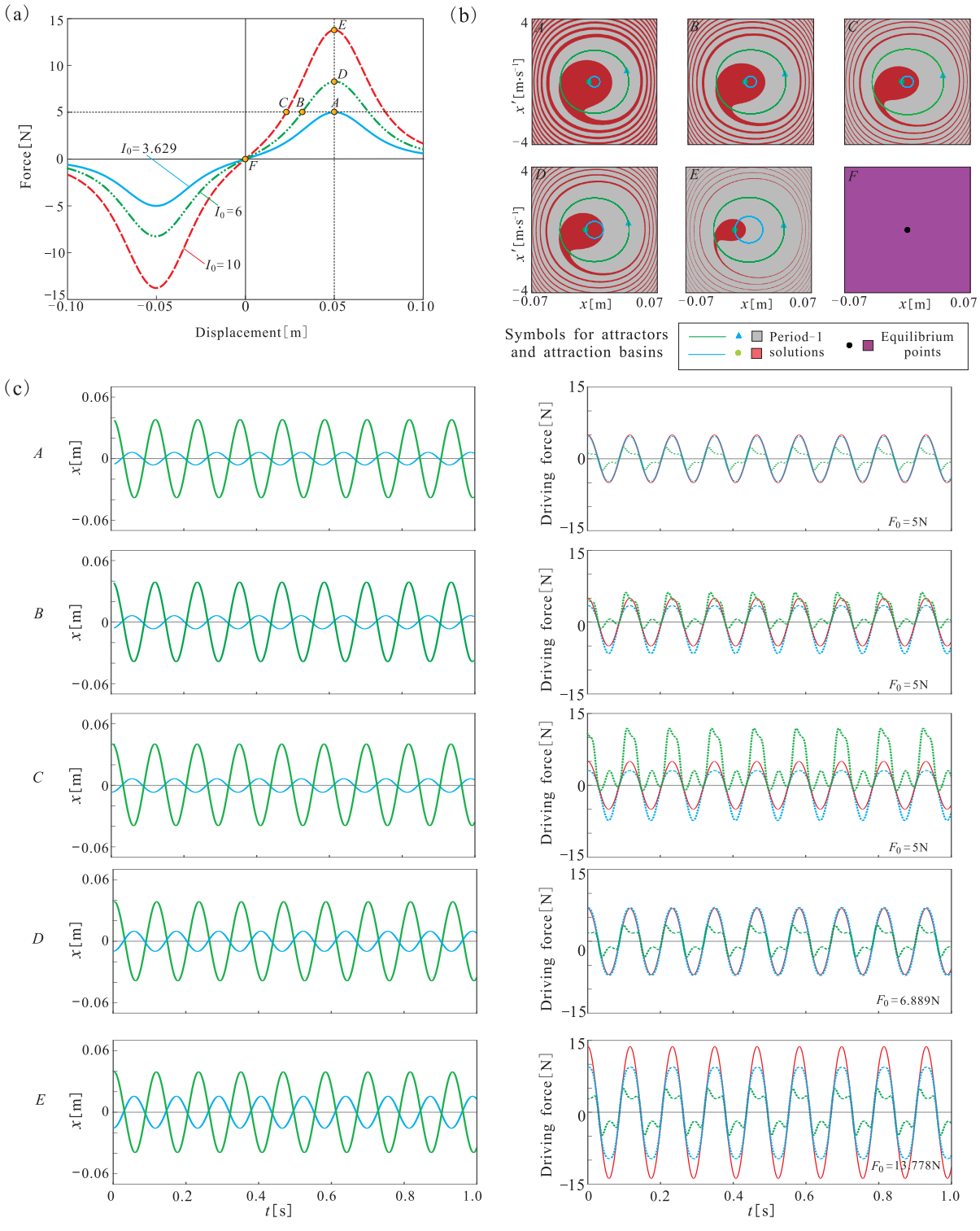

Figure 12: (colour online) (a) Electromagnetic forces of the single solenoid actuator with parameters D_1=0.05 m, D_2=0.06 m, L=0.10 m, d_1=0.006 m, d_2=0.02 m, l=0.02m. (b) Basins of attraction and phase portraits of the MM oscillator for harmonic input currents in solenoid of the current intensity I_0 and the frequency Ω=54 rad/s, where the magnet locates at positions that are marked by corresponding letters in (a) and the seventh order model of beam structure is adopted (see Figure 5). (c) Time histories of dynamic response shown in (b) and their corresponding electromagnetic driving forces, where the time histories of driving force are plotted by using the same colour with response curves, and meanwhile the ideal harmonic force curves are plotted in red solid curves for the marked point in (a).

4.2. Nonlinear dynamic analysis

The nonlinear dynamic analysis is carried our by a suite of techniques including the Harmonic Balance Method (HBM), path following and direct numerical integration, where the last is used to assess the accuracy of the other methods. The amplitude-frequency curves are computed by the HBM and path following. Furthermore, bifurcation analysis of the MM oscillator subjected to different types of electromagnetic excitations, such as harmonic, parametric and harmonic-parametric excitations, is carried out. These three types of excitations are often used to study linear and nonlinear vibration systems.

First we investigate dynamic behaviour of the MM oscillator excited harmonically with $F_{\mathrm{m}} = F\cos(\Omega t)$ is firstly discussed, which corresponds to $f_{\mathrm{m}} = f\cos(\omega\tau)$ in Eq. (20). When applying the HBM, the solution of Eq. (20) is assumed to be $x = A\sin\omega\tau + B\cos\omega\tau$. This solution is substituted into the equation of motion leading to a long expression given in Appendix C. By letting coefficients of terms $\cos(\omega\tau)$ and $\sin(\omega\tau)$ be equal to zero, two following amplitude-frequency equations are obtained

$$\begin{cases} 35b_7B^7 + 105b_7A^2B^5 + 105b_7A^4B^3 + 35b_7A^6B + 40b_5B^5 + 80b_5A^2B^3 + 40b_5A^4B + \\ 48b_3B^3 + 48b_3A^2B - 64\omega^2B + 64B + 64\zeta\omega A - 64f = 0, \\ 35b_7AB^6 + 105b_7A^3B^4 + 105b_7A^5B^2 + 35b_7A^7 + 40b_5AB^4 + 80b_5A^3B^2 + 40b_5A^5 + \\ 48b_3AB^2 + 48b_3A^3 - 64\zeta\omega B - 64\omega^2A + 64A = 0. \end{cases} \tag{21}$$

These algebraic equations are solved by using the Newton-Raphson iteration algorithm and arc-length continuation method, and later the Floquet theory is employed to analyze the stability of periodic solutions obtained by the HBM [14, 86–88]. Consequently, Figure 13 is computed showing the amplitude-frequency response curve for F=5.0 N and C=0.5 N $\cdot$ m/s.

In order to asses the optimization process presented in Subsection 3.3, the same parameters as in Figure 11(e) are used, while the frequency of the input current is chosen at Ω=60 rad/s, which is the resonant frequency as presented in Figure 13. Figures 14(a) and 14(d) show phase portraits obtained for the harmonic force, 5 cos(60t), the electromagnetic forces with the same parameters as those for Figure 11(e) and the current frequency of 60 rad/s. The phases trajectories shown in 14(a), which are almost identical, are obtained for the corresponding excitation forces presented in Figure 14(b). Figure 14(c) presents the variances between the driving forces and the harmonic force, namely the former minus the latter, which indicates that the quasi-constant force type is the best choice with a maximum variance of about 1.1×10^{-5} N, and the double peak force is also good with a small variance of 0.02736 N, while the single peak force has a big variance of 0.7332 N. A similar pattern is manifested by the oscillator for Figures 14(e) and 14(f). In the case of large amplitudes which correspond to large deflection of the beam structure with a maximum amplitude of about 0.0569 m,

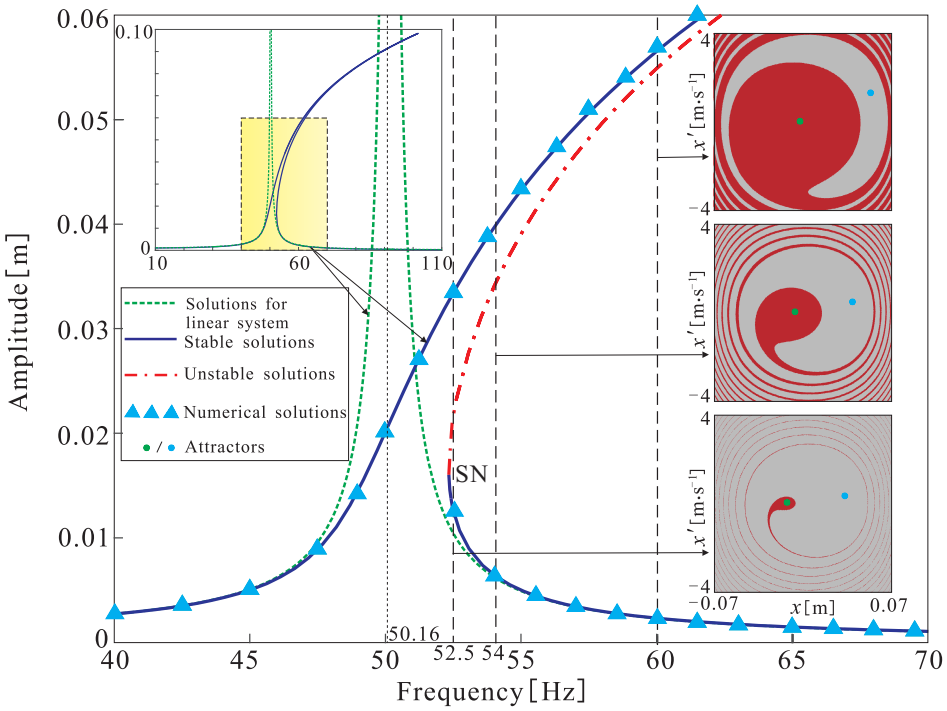

Figure 13: (colour online) The amplitude-frequency response curves for linear (green) and nonlinear (blue and red) cases together with basins of attraction computed for three frequencies of 52.5, 54.0, 60.0 rad/s.

the variances for the double peak, quasi-constant and the single peak forces at resonance are 0.0258 N, 0.1643 N and 0.6990 N, respectively. In this case, the maximum relative error of the double peak force is only 0.516%, while it is 3.286% for the quasi-constant force. In conclusion, the quasi-constant force type can generate a harmonic force for oscillations with designed small amplitudes. In addition, it is an effective method to extend the range of nearly constant force to tune the parameter d to transform the quasi-constant force into a weak double peak force.

Next, bifurcation analysis of the magneto-mechanical oscillator is undertaken for the simplified model described by Eq. (17) and compared with the original model, namely Eq. (15). This corresponds to the physical configuration where if the magnet being placed in the middle point of the single solenoid actuator, then F_0=0, else F_0 is nonzero. Figure 15(a) depicts the bifurcation diagrams for the displacement x versus I_0 and G_1 for the original model and the simplified model, where the driving forces are expressed by Eqs (15) and (17), respectively. The other parameters used in Figure 15 as same as those in Figure 8 and Ω=54 rad/s. Figure 15(a) indicates that the simplified model is in a good agreement with the original model. The phase portraits of the oscillator for I_0=6 A and the corresponding G_1=1680.7 N/m further validate this point. In this figure we see a pair of saddle-node (SN) bifurcations occurring at about I_0=2.94 A, which means G_1=817.74 N/m, where the stable and unstable period-1 solutions are paired up. It should be pointed out that the description of bifurcation

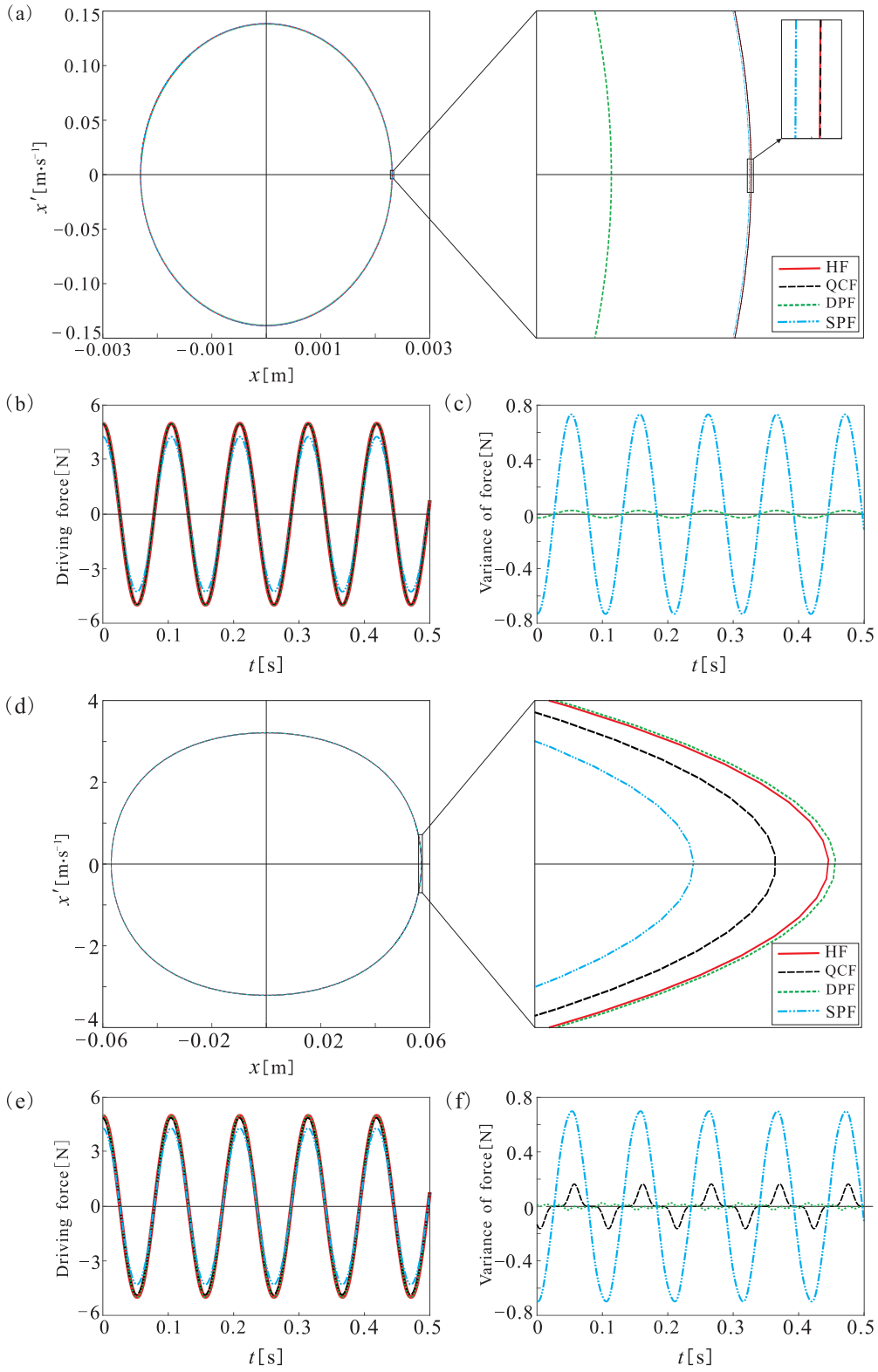

Figure 14: (colour online) Comparisons of responses of the magneto-mechanical oscillator under the configures of the quasi-constant force, the double peak force, the single peak force as well as driven by the desired harmonic force: (a) and (d) the non-resonant and resonant trajectories, respectively, (b) and (e) the driving forces for corresponding trajectories in (a) and (d), (c) and (f) the variances of driving forces compared with the harmonic force.

scenarios and the method of attraction basin analysis used in this paper are similar to the approach taken in [14, 85].

Figure 15(b) shows that the bifurcation diagram of the simplified model subjected to harmonic-parametric excitations, where F_0=5 N and Ω=54 rad/s and G_1 varies. It can be observed that at small G_1 an unstable and two stable periodic solutions co-exist, for instance, when G_1=0 N/m, that is, only driven by the harmonic excitation, the frequency response curve in Figure 13 confirms the same frequency of Ω=54 rad/s. When increasing G_1 to 1644.16 N/m, a saddle-node bifurcation occurs accompanying with a pair of stable and unstable period-1 solutions.

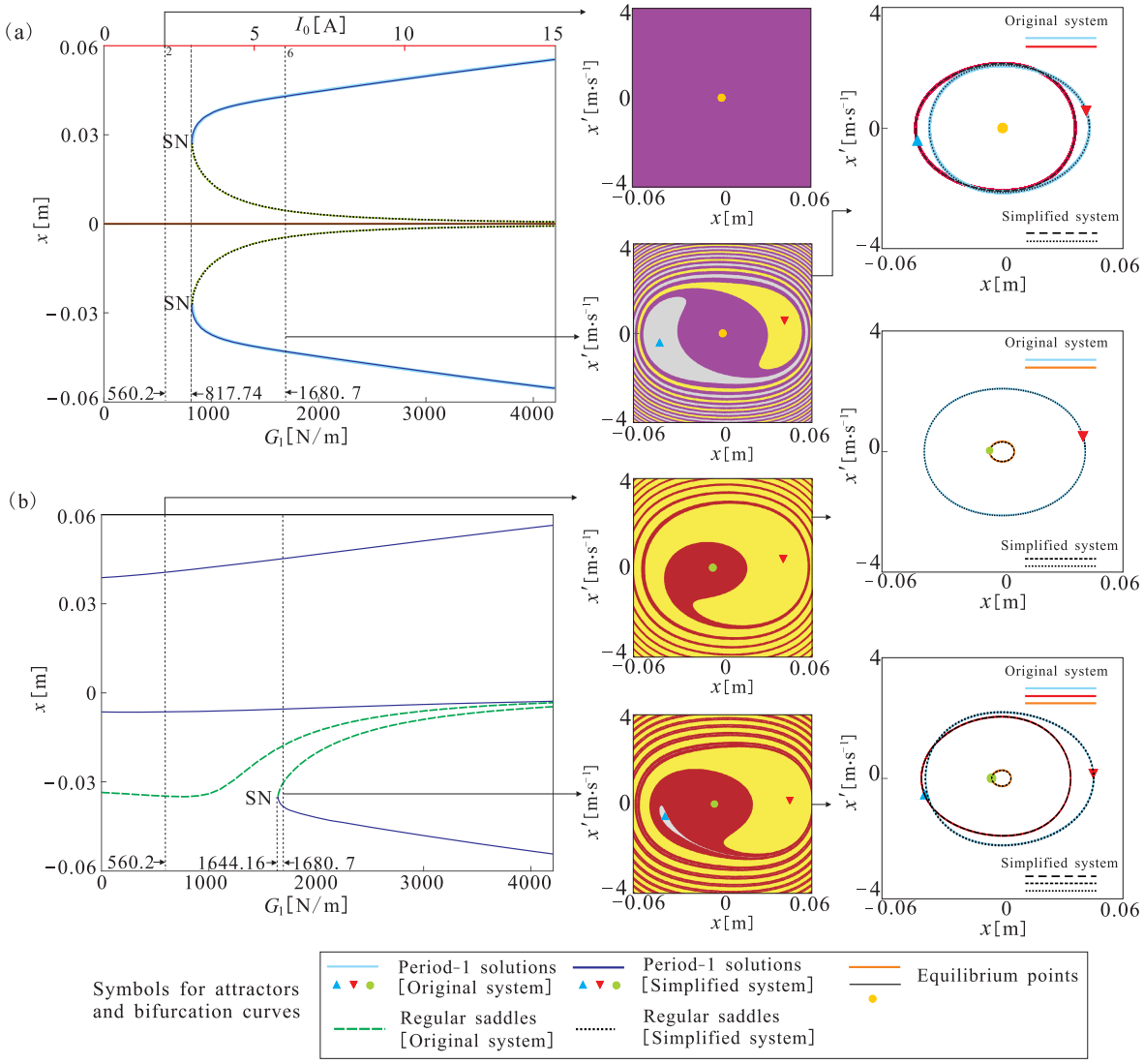

Figure 15: (colour online) Bifurcation diagrams of the MM oscillator calculated for Ω=54 rad/s and for (a) the original and simplified system together, where the magnet is placed at the centre of the solenoid and I_0 and G_1 are branching parameters, respectively; (b) the simplified system, where F_0=5 N and G_1 is a branching parameter.

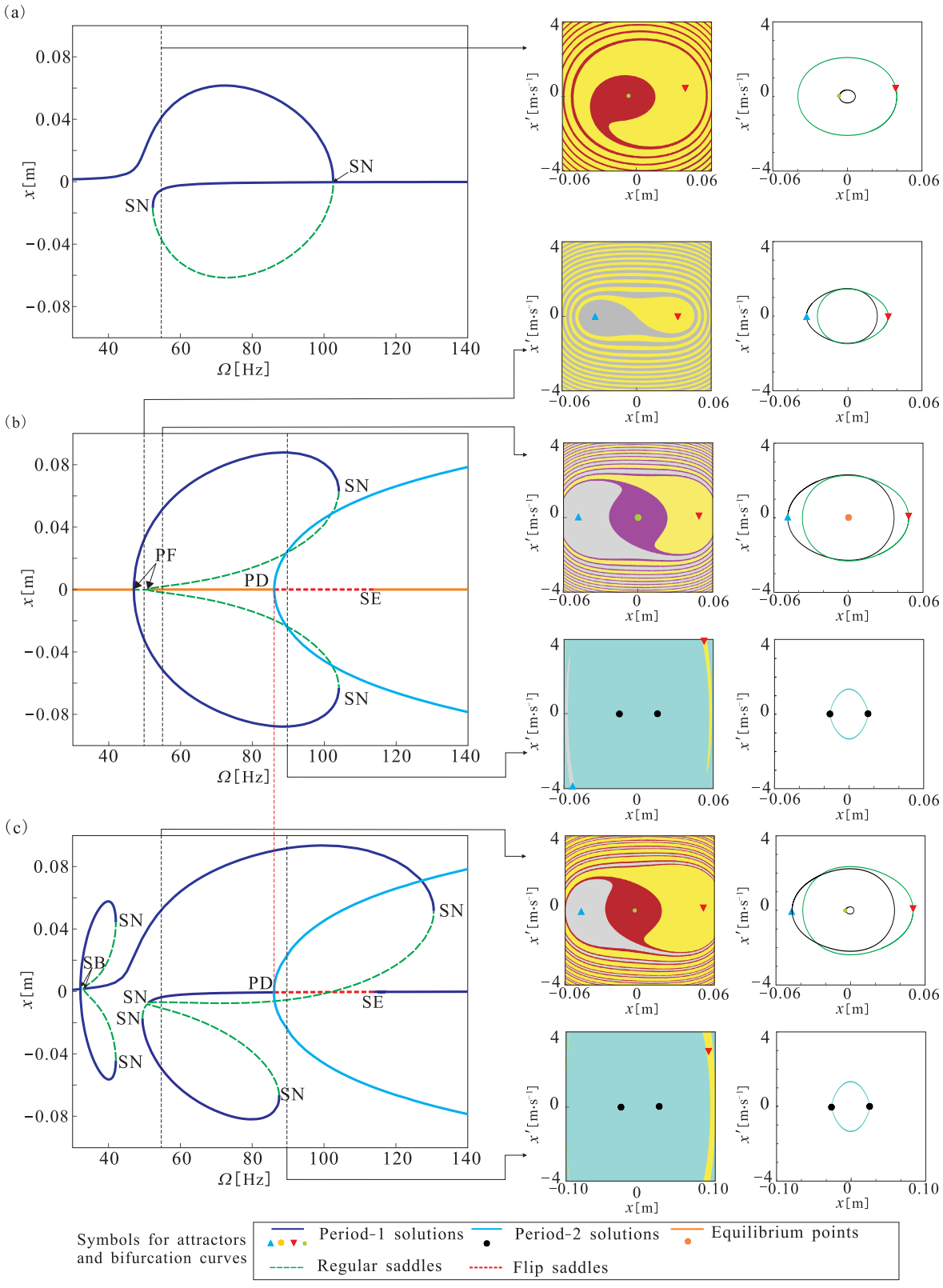

Figure 16: (colour online) Bifurcation diagrams of x versus Ω of the simplified MM system calculated for harmonic, parametric and harmonic-parametric EM driving forces: (a) F_0=5.0 N, G_1=0.0 N/m, (b) F_0=0.0 N, G_1=2801.2 N/m, (c) F_0=5.0 N, G_1=2801.2 N/m.

In addition to effects of the force amplitude which are directly related to the above-mentioned input current intensity, Figure 16 presents the bifurcations with respect to the excitation frequency, which are vital to understand the global dynamic behaviour. Figure 16(a) shows the bifurcation diagram of x versus Ω for the harmonic forcing, F=5.0 cos(Ωt), which describes the same bifurcation scenario as in Figure 13, that is, two saddle-node (SN) bifurcation points at 52.33 rad/s and 102.59 rad/s, which correspond to jump-up and jump-down frequencies when the frequency is swept. Figure 16(b) depicts that the bifurcation diagram for the case of the parametric excitation, F=2801.2x cos(Ωt), indicating the system can not oscillate at the lower frequency than the pitch-fork (PF) bifurcation frequency 46.95 rad/s, and through this bifurcation, a pair of stable period-1 solutions is born. The pair of period-1 orbits disappear via the SN bifurcations at around 104.06 rad/s. There still exists another PF bifurcation at about 50.79 rad/s and a period-doubling (PD) bifurcation at about 86.05 rad/s. Last but not least, a special bifurcation, called a stability exchange (SE) bifurcation herein, occurs at 113.75 rad/s, where a flip saddle becomes a stable equilibrium. Figure 16(c) shows the bifurcation scenarios for the harmonic-parametric excitation F=(5.0+2801.2x) cos(Ωt) and when compared to the two previously discussed cases, presents richer bifurcation scenarios. Firstly, the two SN bifurcations shown panel (a) still exist, and secondly, the PD bifurcation and the stability bifurcation are preserved at almost the same frequencies as in panel (b). Different from the above two bifurcations, there are two symmetry breaking (SB) bifurcations at 32.18 rad/s and 33.11 rad/s and other four SN bifurcations at 42.05 rad/s, 42.05 rad/s, 49.47 rad/s and 87.52 rad/s, respectively.

5. Experimental validation of MM oscillator model

In this section, we aim to provide an experimental validation of the developed model of the MM oscillator, which is based on the recent studies undertaken in the Centre for Applied Dynamics Research (CADR) at the University of Aberdeen [78, 79]. Figure 1 shows the experimental apparatus and its physical model, where the main parameters are D_1=0.03 m, D_2=0.044 m, L=0.05 m, d_1=0.006 m, d_2=0.02 m, l=0.02 m. In addition, the distance of the centre of the magnet in relation to the centre of the coil is denoted as d_c. The effective length, width and thickness of each leaf spring in the experimental MM oscillator are 125 mm, 40 mm and 0.5 mm, respectively, and the total mass of the lumped mass together with the magnet and the steel linked rod is 1.325 kg.

Panels of Figure 17 explains the adopted approach, where the full nonlinear force-displacement curves, the calibrated force-current relationship, the time history of input current and the comparison between experimental and predicted generated force are shown in subsequent panels. The empirical formula for the electromagnetic force F and the input current I, that is, $F_{\text{coil}}(t) = aI(t)$, where a=0.799 was experimentally obtained and is valid for alternating input currents with amplitudes up to 2.5 A and frequencies from 6 to 10 Hz. Figure 17(a) shows a series of analytical curves computed using Eq.

(15) for electromagnetic force versus constant currents for I=0.1 A and increasing it from 0.5 A to 5 A by 0.5 A. The red dashed line denotes the rest position the magnet in the coil with $d_c = 11$ mm, and the green crosses marked electromagnetic forces corresponding to different values of current I. Figure 17(b) compares the analytical and experimental electromagnetic forces under various currents marked with green crosses and red solid dots, respectively. Figures 17(c) and (d) show the time histories of the input alternating current and the corresponding electromagnetic force. The predicted force is also plotted in panel (d) with red dashed lines, which indicates that the analytical results are in a good agreement with the experimental counterparts.

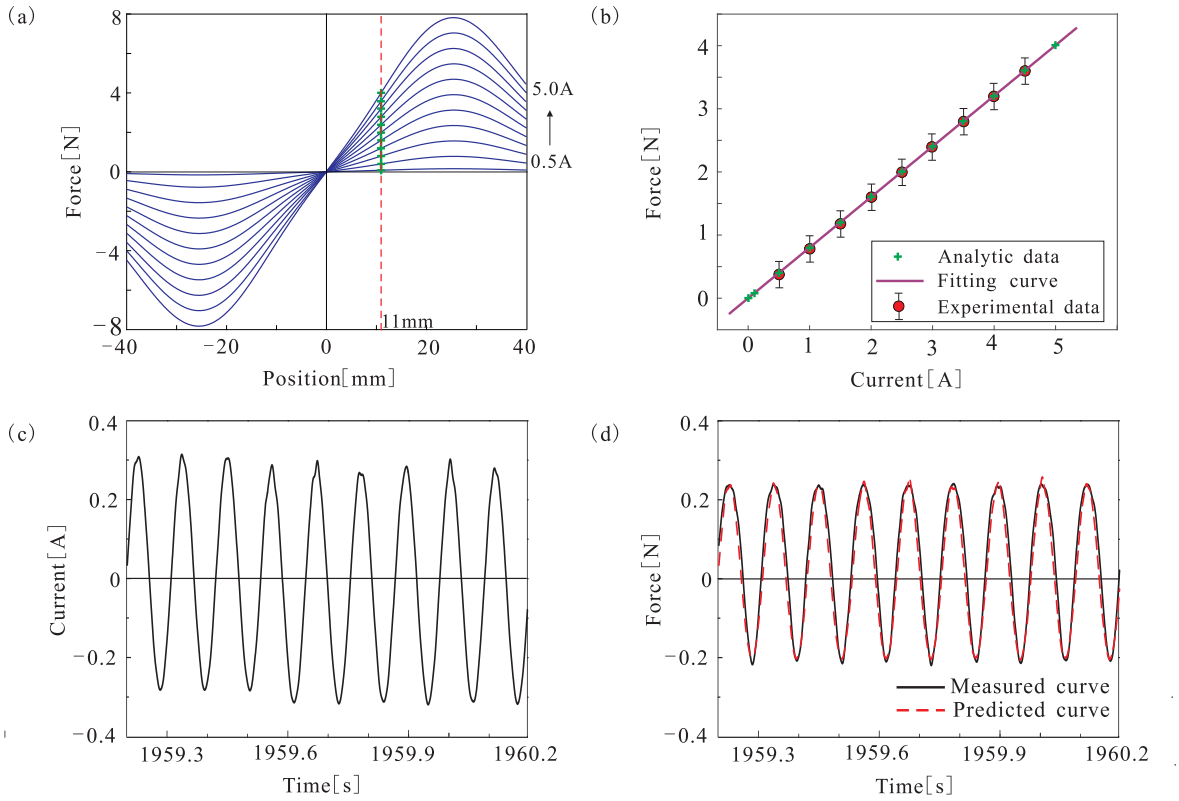

Figure 17: (colour online) Calibration of force versus current dependency: (a) analytical electromagnetic force computed for current I=0.1 A increasing the input current from 0.5 A to 5 A by 0.5 A; (b) measured and analytical force versus static current at the rest position marked with red dots and green crosses, respectively, where the fit line is plotted in purple for analytical curve with the coefficient 0.802; (c) input current time histories; (d) measured and predicted force time histories corresponding to the input current in (c) plotted in black solid and red dashed curves, respectively.

Figure 18 depicts the response characteristics of the MM oscillator under the alternating current input, that is, $I = I_0\cos(\omega t)$, where I_0=0.40 A. A sweep frequency experiment is implemented by increasing and decreasing frequencies from 6 Hz to 10 Hz and from 10 Hz to 6 Hz, for which the amplitude-frequency (AF) responses are marked with black circles and red asterisk, respectively. To calculated the AF curves analytically, the linear and nonlinear stiffness models of the parallel leaf

springs are firstly constructed by using the method in Section 2.

The analytical study proves that the cubic model is good enough to describe the stiffness of the MM oscillator when the amplitude of vibration is smaller than 20 mm. Without the mass considered, the coefficients are $K_1 = 4.3009 \times 10^3$ N/m and K_3= 4.5807×10^5 N/m^3 and $K_1 = 4.2995 \times 10^3$ N/m and K_3= 5.1232×10^5 N/m^3 when data in vibration amplitude 1.5 mm and 20 mm are taken, respectively. The fit results are in keeping with the traditional linear and cubic nonlinear results obtained from Eq. (B.3), which gives $K_1 = 4.3008 \times 10^3$ N/m and K_3= 2.8312×10^5 N/m^3. In the case of the mass influence considered, the coefficients are $K_1 = 4.4255 \times 10^3$ N/m, K_3= 5.6013×10^5 N/m^3 and $K_1 = 4.4256 \times 10^3$ N/m, K_3= 5.2282×10^5 N/m^3, when those data in vibration amplitudes of 1.5 mm and 20 mm are adopted, respectively. However, it should be pointed out that the machining accuracy for the beam can have a strong influence on its real stiffness. Hence, to calibrate the theoretical result, Figure 18 will adopt $K_1 = 4.331 \times 10^3$ N/m and $K_3 = 5.2 \times 10^5$ N/m^3 as linear and cubic stiffness coefficients and C=0.27 kg/s^2, of which the linear stiffness coefficient and the damping coefficient are derived experimentally to see [79] for details.

It is shown that the analytical results of the linear and nonlinear AF curves are in a good agreement with the experimental results except for at resonant frequencies, e.g., 9.1 Hz and 9.2 Hz. Hence, Figure 18 further compares the phase trajectories for those two frequencies to show the experimental and numerical results by using the electromagnetic force model and the harmonic force model, that is, Eq. (15) and $F_{\mathrm{m}} = F\cos(\Omega t)$. The numerical trajectories are in good agreement with the experimental results at 9.1 Hz and for the case of small amplitude of co-existing responses at 9.2 Hz. However, for the large amplitude of phase trajectory at 9.2 Hz, Figure 18 shows that the numerical results for selected cubic stiffness $K_3 = 5.2 \times 10^5$ N/m^3 and $K_3 = 7.6 \times 10^5$ N/m^3, which cannot match with the experimental result well enough in shape and is worthy of further study.

6. Conclusions

This paper presents a new magneto-mechanical oscillator model focusing on the large-deflection of parallel leaf springs and the electromagnetic actuator. We proposed a new analytical approach describing the large deflection beam, where the equilibrium equation was transformed into a boundary value problem, from which the formulas for the restoring force were derived. The final mathematical expression for the restoring force dependent on the deflection was obtained by the least square polynomial fit method.

The model describing magnetic forces generated by a single solenoid actuator was developed by using the infinitesimal element analysis method and the charge model. It was found that the electromagnetic force of the single solenoid actuator strongly depends on the position of the permanent

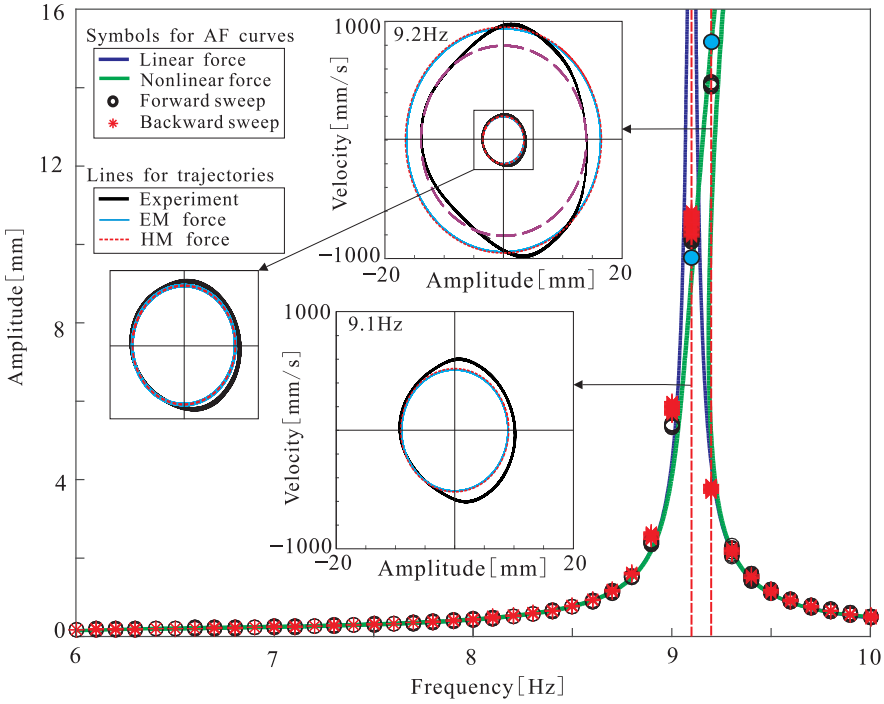

Figure 18: (colour online) Amplitude-frequency (AF) Responses at $I_0 = 0.40$ A : experimental, analytical, and numerical results are shown comparatively, where the used corresponding symbols are marked right-upper side in the panel. Experimental amplitudes of responses are obtained by increasing (forward sweep) and decreasing (backward sweep) excitation frequency, which are marked with black circles and red asterisk, respectively. EM and HM forces denote electromagnetic and harmonic force models. The nonlinear amplitude-frequency curve and numerical trajectories at 9.1 Hz and 9.2 Hz are plotted for stiffness coefficients $K_1 = 4.331 \times 10^3$ N/m and $K_3 = 5.2 \times 10^5$ N/m^3. In addition, the co-existing orbits computed at 9.2 Hz for $K_1 = 4.331 \times 10^3$ N/m and $K_3 = 7.6 \times 10^5$ N/m^3 is also plotted with a purple long dashed line. Numerical response amplitudes at 9.1 Hz and 9.2 Hz are also marked with cyan solid dots that are in a good agreement with analytical results.

magnet in the solenoid, so it cannot supply a purely harmonic excitation for large oscillation amplitudes.

Another contribution of this paper is a new design of an electromagnetic actuator with a pair of identical solenoids. The new concept of the quasi-constant force (QCF) was introduced to generate a nearly constant amplitude excitation when passing constant current through the solenoid. Hence, the twin-solenoids actuator with the QCF design can supply a wide range of excitations, for instance, a harmonic alternating input current can generate a harmonic excitation and similarly a stochastic current would generate a stochastic excitation. To widen the QCF region, an optimization procedure was carried out for the new design, which found that by increasing the lengths, inner and outer diameters of the solenoids can broaden the QCF range. The study demonstrated that the electromagnetic force curves can be classified into four kinds of segments by considering their local geometry, that is, the quasi-constant, linear, single-peak and double-peak forces. The four local forces can also be modelled with polynomials. Furthermore, the effective constant force range can be improved by a fine adjustment of the distance between the pair of solenoids, which changes the quasi-constant force into the weak double peak force.

The dependency between the electromagnetic driving forces and the position of magnet in the actuator was discussed and its effect on the system dynamics was examined by constructing basins of attraction and phase portraits for various types of excitations. The obtained amplitude-frequency response curves computed for a harmonic excitation showed the classical nonlinear resonance phenomena, which were further investigated via the bifurcation analysis for the original and simplified electromagnetic excitations, where rich bifurcation scenarios were observed. Last but not least, a short experimental validation of our theoretical models was given showing a good agreement between the developed model and the previous experiments.

CRediT authorship contribution statement

Zhifeng Hao: Conceptualization, Investigation, Methodology, Software, Writing-original draft, Writing-review & editing. Dan Wang: Conceptualization,Investigation, Methodology, Software, Writing-original draft, Writing-review & editing. Marian Wiercigroch: Supervision, Conceptualization, Methodology, Writing-review & editing.

Declaration of Competing Interest

The authors declare that they have no known competing financial interests or personal relationships that could have appeared to influence the work reported in this paper.

Acknowledgement

ZH and DW acknowledge the financial supports of CSC (China Scholarship Council) and the Natural Science Foundation of Shandong Province (No.ZR2017BA031, ZR2017QA005), the National Natural Science Foundation of China (No.11702111, 11732014). The authors also thank Drs Dimitri Costa and Vahid Vaziri for their experimental support.

Appendix

Appendix A. Constitutive relations of beam structure

The relationships between the bending angular θ and the deflection ω of beam

$$\begin{aligned} &\omega' = \tan\theta, \\ &\cos\theta = \frac{1}{\sqrt{1+\tan^2\theta}} = \frac{1}{\sqrt{1+\omega'^2}}, \\ &\sin\theta = \cos\theta\tan\theta = \frac{\omega'}{\sqrt{1+\omega'^2}}. \end{aligned} \tag{A.1}$$

Additionally, taking the first order approximation of $M(s+\mathrm{d}s)$ and $Q(s+\mathrm{d}s)$ and neglecting the higher orders, that is,

$$\begin{aligned} &M(s+\mathrm{d}s) = M(s) + \mathrm{d}M, \\ &Q(s+\mathrm{d}s) = Q(s) + \mathrm{d}Q, \\ &M(s+\mathrm{d}s) - M(s) - (Q+\mathrm{d}Q)\mathrm{d}s = 0, \end{aligned} \tag{A.2}$$

it can derive out that

$$Q = \frac{\mathrm{d}M}{\mathrm{d}s}. \tag{A.3}$$

Appendix B. Stiffness formula of beam structure in small deflection

Consider the entire parallel leaf spring beam as a free body by referring to [46], shown in Figure B.1, the reaction of the beam at O is $-P$. Cut through the beam at a point K with a distance x from the fixed end O, and then see the left-hand side part of the beam as a free body. Consider the equilibrium equations of the body, the shear force P and bending moment m at K satisfy

$$\begin{aligned} &M(x) = -Px - (-PL - m), \\ &\theta(x) = \tfrac{1}{EI}[\tfrac{-P}{2}x^2 - (-PL-m)x + C], \\ &\omega(x) = \tfrac{1}{EI}[\tfrac{-P}{6}x^3 - \tfrac{1}{2}(-PL-m)x^2 + Cx + D], \end{aligned} \tag{B.1}$$

where $M(x), \theta(x)$ and $\omega(x)$ are the bending moment, the rotation angular and the deflection, respectively. Note the boundary conditions of parallel leaf spring beam are $\omega(0) = 0, \theta(0) = 0, \theta(L) = 0$,

hence it can be derived out from Eq. (B.1) that $D = 0, C = 0, m = -\frac{PL}{2}$, and $\omega(L) = \frac{PL^3}{12EI}$. Hence, the stiffness of the moving end of the parallel spring beam under small deflection can be expressed as

$$k = \frac{P}{\omega(L)} = \frac{12EI}{L^3}. \tag{B.2}$$

Another result in literature [60] presents the dynamic stiffness of the beam of parallel leaf springs is

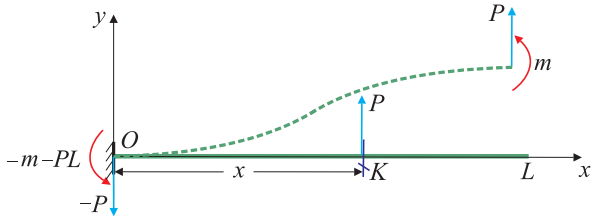

Figure B.1: Shear-force and bending-moment diagram for a simplified parallel leaf spring beam with a concentrated load P.

$$k(x) = 12\frac{EI}{L^3} + \frac{1296}{35}\frac{EI}{L^5}x^2, \tag{B.3}$$

which considers the cumulative effect of nonlinearity of beam and retains the first two terms of Taylor series for $\sin\theta$, namely $\theta - \frac{\theta^3}{6}$, instead of only the linear term, where θ is the inclination angle of the beam section. The nonlinear formulas is more precise than the above-mentioned linear result in a relative large deflection.

Appendix C. Equations for harmonic solutions

$$\begin{aligned}
&(\tfrac{3}{4}\,b_3B^3 + \tfrac{5}{4}\,b_5A^2B^3 + \tfrac{105}{64}\,b_7A^2B^5 + \tfrac{105}{64}\,b_7A^4B^3 + \tfrac{5}{8}\,b_5B^5 + \tfrac{35}{64}\,b_7A^6B + \tfrac{35}{64}\,b_7B^7 + \tfrac{3}{4}\,b_3A^2B - \\
&B\omega^2 + \tfrac{5}{8}\,b_5A^4B + \zeta\,A\omega + B - f)\cos(\omega\,t) + (\tfrac{35}{64}\,b_7A^7 + \tfrac{35}{64}\,b_7AB^6 + \tfrac{105}{64}\,b_7A^5B^2 + \tfrac{5}{8}\,b_5A^5 + \\
&\tfrac{5}{8}\,b_5AB^4 + \tfrac{105}{64}\,b_7A^3B^4 + \tfrac{5}{4}\,b_5A^3B^2 + \tfrac{3}{4}\,b_3AB^2 + \tfrac{3}{4}\,b_3A^3 - \zeta\,B\omega - A\omega^2 + A)\sin(\omega\,t) + \\
&(\tfrac{5}{8}\,b_5A^3B^2 + \tfrac{15}{16}\,b_5AB^4 + \tfrac{3}{4}\,b_3AB^2 - \tfrac{1}{4}\,b_3A^3 - \tfrac{5}{16}\,b_5A^5 + \tfrac{63}{64}\,b_7AB^6 + \tfrac{105}{64}\,b_7A^3B^4 - \tfrac{21}{64}\,b_7A^7 + \\
&\tfrac{21}{64}\,b_7A^5B^2)\sin(3\,\omega\,t) + (\tfrac{21}{64}\,b_7B^7 - \tfrac{105}{64}\,b_7A^4B^3 + \tfrac{1}{4}\,b_3B^3 - \tfrac{15}{16}\,b_5A^4B - \tfrac{63}{64}\,b_7A^6B - \tfrac{3}{4}\,b_3A^2B + \\
&\tfrac{5}{16}\,b_5B^5 - \tfrac{21}{64}\,b_7A^2B^5 - \tfrac{5}{8}\,b_5A^2B^3)\cos(3\,\omega\,t) + \\
&(\tfrac{1}{16}\,b_5B^5 + \tfrac{35}{64}\,b_7A^6B + \tfrac{7}{64}\,b_7B^7 - \tfrac{63}{64}\,b_7A^2B^5 - \tfrac{5}{8}\,b_5A^2B^3 + \tfrac{5}{16}\,b_5A^4B - \tfrac{35}{64}\,b_7A^4B^3)\cos(5\,\omega\,t) + \\
&(\tfrac{1}{16}\,b_5A^5 + \tfrac{7}{64}\,b_7A^7 + \tfrac{35}{64}\,b_7AB^6 - \tfrac{5}{8}\,b_5A^3B^2 - \tfrac{35}{64}\,b_7A^3B^4 + \tfrac{5}{16}\,b_5AB^4 - \tfrac{63}{64}\,b_7A^5B^2)\sin(5\,\omega\,t) + \\
&(-\tfrac{7}{64}\,b_7A^6B + \tfrac{35}{64}\,b_7A^4B^3 + \tfrac{1}{64}\,b_7B^7 - \tfrac{21}{64}\,b_7A^2B^5)\cos(7\,\omega\,t) + \\
&(-\tfrac{1}{64}\,b_7A^7 - \tfrac{35}{64}\,b_7A^3B^4 + \tfrac{7}{64}\,b_7AB^6 + \tfrac{21}{64}\,b_7A^5B^2)\sin(7\,\omega\,t) = 0.
\end{aligned} \tag{C.1}$$

References

[1] Xu X, Wiercigroch M. Approximate analytical solutions for oscillatory and rotational motion of a parametric pendulum. Nonlinear Dyn 2007; 47: 311-420.

[2] Guo C, Luo ACJ, Periodic motions on bifurcation trees in an inverted pendulum with a periodically moving base. Int J Control 2021; 9: 410-423.

[3] Han N, Lu PP, Li ZX. An approximate technique to test chaotic region in a rotating pendulum system with bistable characteristics. Nonlinear Dyn 2021; 104: 191-214.

[4] Ueda Y. Randomly transitional phenomena in the system governed by Duffings equation. J Stat Phys 1979; 20: 181-196.

[5] Chen B, Huang J, Ji JC. Control of flexible single-link manipulators having Duffing oscillator dynamics. Mech Syst Signal Process 2019; 121(15): 44-57.

[6] Hou L, Su XC, Chen YS. Bifurcationmodes of periodic solution in a Duffing system under constant force as well as harmonic excitation. Int J Bifurcat Chaos 2019; 29(13): 1950173.

[7] Tian RL, Zhao ZJ, Xu Y. Variable scale-convex-peak method for weak signal detection, Sci China Technol Sc 2021; 64(2): 331-340.

[8] Lorenz EN. Deterministic nonperiodic flow. J. Atmos. Sci. 2004; 20:130-141.

[9] Lü J, Chen G, Cheng D, Celikovsky S. Bridge the gap between the Lorenz system and the Chen system. Int J Bifurcat Chaos 2002; 12(12): 2917-2926.

[10] Zhao X, Liu J, Mou J, Ma CG, Yang FF. Characteristics of a laser system in complex field and its complex self-synchronization, Eur Phys J Plus 2020; 135(6): 507.

[11] Cao QJ, Wiercigroch M, Pavlovskaia EE, Grebogi C, Thompson JMT. Piecewise linear approach to an archetypal oscillator for smooth and discontinuous dynamics. Philos Trans R Soc A 2008; 366: 635-652.

[12] Hao Z, Cao Q. A novel dynamical model for GVT nonlinear supporting system with stable-quasi-zero-stiffness. J Theor App Mech-Pol 2014; 52(1): 199-213.

[13] Li Z, Cao Q, Nie Z. Stick-slip vibrations of a self-excited SD oscillator with Coulomb friction. Nonlinear Dyn 2020; 102:1419-1435.

[14] Hao Z, Cao Q, Wiercigroch M. Two-sided damping constraint control strategy for high-performance vibration isolation and end-stop impact protection. Nonlinear Dyn 2016; 86: 2129-2144.

[15] Zhang YX, Luo GW. Multistability of a three-degree-of-freedom vibro-impact system. Commun Nonlinear Sci Numer Simulat 2018; 57:331-341.

[16] Lai ZH, Thomson G, Yurchenko D, Val DV, Rodgers E. On energy harvesting from a vibro-impact oscillator with dielectric membranes. Mech Syst Signal Process 2018; 107: 105-121.

[17] Guo B, Chávez J, Liu Y, Liu C. Discontinuity-induced bifurcations in a piecewise-smooth capsule system with bidirectional drifts Commun Nonlinear Sci Numer Simulat 2021; 102: 105909.

[18] Li G, Yue Y, Xie JH, Grebogi C. Strange nonchaotic attractors in a nonsmooth dynamical system. Commun Nonlinear Sci Numer Simulat 2019; 78: 104858.

[19] Ibrahim RA. Recent advances in nonlinear passive vibration isolators. J Sound Vib 2008; 314(3-5): 371-452.

[20] Hao Z, Cao Q. The isolation characteristics of an archetypal dynamical model with stable-quasi-zero-stiffness. J Sound Vib 2015; 340:61-79.

[21] Lu Z, Wang Z, Zhou Y, Lu X. Nonlinear dissipative devices in structural vibration control: A review. J Sound Vib 2018; 423: 18-49.

[22] Ledezma-Ramírez DF, Tapia-González PE, Ferguson N, Brennan M, Tang B. Recent Advances in Shock Vibration Isolation: An Overview and Future Possibilities. Appl Mech Rev 2019; 71(6): 060802.

[23] Wang Y, Jing XJ, Dai H, Li FM. Subharmonics and ultra-subharmonics of a bio-inspired nonlinear isolation system. Int J Mech Sci 2019; 152: 167-184.

[24] Liu CR, Yu KP. Accurate modeling and analysis of a typical nonlinear vibration isolator with quasi-zero stiffness. Nonlinear Dyn 2020, 100: 2141-2165.

[25] Liu CR, Yu KP, Liao BP, Hu RP. Enhanced vibration isolation performance of quasi-zero-stiffness isolator by introducing tunable nonlinear inerter. Commun Nonlinear Sci Numer Simul 2021; 95: 105654.

[26] Kandasamy R, Cui F, Townsend N, Foo C, Guo J, Shenoi A, Xiong Y. A review of vibration control methods for marine offshore structures. Ocean Eng 2016; 127(15): 279-297.

[27] Brzeski P, Lazarek M, Perlikowski P. Experimental study of the novel tuned mass damper with inerter which enables changes of inertance. J Sound Vib 2017; 404(15): 47-57.

[28] Meng H, Sun XT, Xu J, Wang F. The generalization of equal-peak method for delay-coupled nonlinear system. Physica D 2020; 403: 132340.

[29] Bian J, Jing XJ. A nonlinear X-shaped structure based tuned mass damper with multi-variable optimization (X-absorber). Commun Nonlinear Sci Numer Simulat 2021; 99: 105829.

[30] Yang Z, Zhou S, Zu J, Inman D. High-Performance Piezoelectric Energy Harvesters and Their Applications. Joule 2018; 2: 1-56.

[31] Safaei M, Sodano HA, Anton SR. A review of energy harvesting using piezoelectric materials: state-of-the-art a decade later (2008-2018). Smart Mater Struct 2019; 28: 113001.

[32] Maamera B, Boughamoura A, El-Bab A, Francis L, Tounsia F. A review on design improvements and techniques for mechanical energy harvesting using piezoelectric and electromagnetic schemes. Energy Convers Manag 2019; 199(1): 111973.

[33] Yang T, Cao QJ, Hao ZF. A novel nonlinear mechanical oscillator and its application in vibration isolation and energy harvesting. Mech Syst Signal Process 2021; 155: 107636.

[34] Wang D, Hao ZF, Chen FQ, Chen YS. Nonlinear energy harvesting with dual resonant zones based on rotating system. Appl Math Mech-Engl 2021; 42(2): 275-290.

[35] Wang K, Ouyang HJ, Zhou JX, Chang YP, Xu DL, Zhao H. A nonlinear hybrid energy harvester with high ultralow-frequency energy harvesting performance. Meccanica 2021; 56(2): 461-480.

[36] Yang T, Cao Q, Li Q, Qiu H. A multi-directional multi-stable device: Modeling, experiment verification and applications. Mech Syst Signal Process 2021; 146: 106986.

[37] Darban H, Luciano R, Caporale A, Fabbrocino F. Higher modes of buckling in shear deformable nanobeam. Int J Eng Sci 2020; 154: 103338.

[38] Davis RB, McDowell MD. Combined Euler column vibration isolation and energy harvesting. Smart Mater Struct 2017; 26: 055001.

[39] Liu X, Huang X, Hua H. On the characteristics of a quasi-zerostiffness isolator using Euler buckled beam as negative stiffness corrector. J Sound Vib 2013; 332: 3359-3376.

[40] Sun XT, Wang F, Xu J. Analysis, design and experiment of continuous isolation structure with local quasi-zero-stiffness property by magnetic interaction. Int J Nonlinear Mech 2019; 116: 289-301.

[41] Huang D, Zhou S, Litak G. Theoretical analysis of multi-stable energy harvesters with high-order stiffness terms. Commun Nonlinear Sci Numer Simul 2019; 69: 270-286.

[42] Fan H, Yang L, Tian Y, Wan Z. Design of metastructures with quasi-zero dynamic stiffness for vibration isolation. Compos Struct 2020; 243(1): 112244.

[43] Hu X, Li Y, Xie X. A study on a U-shaped piezoelectric coupled beam and its corresponding ingenious harvester. Energy 2019; 185: 938-950.

[44] Yao MH, Ma L, Zhang W. Study on power generations and dynamic responses of the bistable straight beam and the bistable L-shaped beam. Sci China Tech Sci 2018; 61: 1404-1416.

[45] Cai CQ, Zhou JX, Wu LC, Wang K, Xu D, Ouyang H. Design and numerical validation of quasi-zero-stiffness metamaterials for very low-frequency band gaps. Compos Struct 2020; 236: 111862.

[46] Goodno BJ, Gere JM. Mechanics of Materials, Ninth Edition, SI. Cengage Learning, Boston; 2018.

[47] Santillan ST, Plaut RH, Witelski TP, Virgin LN. Large oscillations of beams and columns including self-weight. Int J Nonlinear Mech 2008; 43(8): 761-771.

[48] Zhou JX, Zhao XH, Wang K, Chang YP, Xu DL, Wen GL. Bio-inspired bistable piezoelectric vibration energy harvester: Design and experimental investigation. Energy 2021; 228: 120595.

[49] Moon FC, Shaw SW. A magnetoelastic strange attractor. J Sound Vib 1979; 65(2): 275-296.

[50] Moon FC, Shaw SW. Chaotic vibrations of a beam with nonlinear boundary-conditions. Int J Nonlinear Mech 1983; 18(6): 465-477.

[51] Ding H, Ji JC, Chen LQ. Nonlinear vibration isolation for fluid-conveying pipes using quasi-zero stiffness characteristics, Mech Syst Signal Process 2019; 121(15): 675-688.

[52] Mao XY, Ding H, Chen LQ. Steady-state response of a fluid-conveying pipe with 3:1 internal resonance in supercritical regime. Nonlinear Dyn 2016; 86: 795-809.

[53] Yan ZM, Sun WP., Tan T, Huang WH. Nonlinear analysis of galloping piezoelectric energy harvesters with inductive-resistive circuits for boundaries of analytical solutions, Commun Nonlinear Sci Numer Simulat 2018; 62: 90-116.

[54] Wang D, Chen YS, Wiercigroch M., Cao QJ. Bifurcation and dynamic response analysis of rotating blade excited by upstream vortices, Appl Math Mech -Engl Ed 2016; 37: 1251-1274.

[55] Wang D, Hao ZF, Pavlovskaia E, Wiercigroch M. Bifurcation analysis of vortex-induced vibration of low-dimensional models of marine risers, Nonlinear Dyn 2021; 106(1): 147-167.

[56] Chen L. An integral approach for large deflection cantilever beams. Int J Nonlin Mech 2010; 45: 301-305.

[57] Yoo CH, Lee S. Stability of structures, Principles and Applications. Butterworth-Heinemann, London; 2011.

[58] Batista M. Analytical treatment of equilibrium configurations of cantilever under terminal loads using Jacobi elliptical functions. Int J Solids Struct 2014; 51: 2308-2326.

[59] Virgin LN, Davis RB. Vibration isolation using buckled struts. J Sound Vib 2003; 260: 965-973.

[60] Emans J, Wiercigroch M., Krivtsov AM. Cumulative effect of structural nonlinearities: chaotic dynamics of cantilever beam system with impacts. Chaos Solitons Fract 2005; 23: 1661-1670.

[61] Nguyen V, Woo K, Pavlovskaia E. Experimental study and mathematical modelling of a new of vibro-impact moling device. Int J Nonlin Mech 2008; 43: 542-550.

[62] Mendrela EA. Comparison of the performance of a linear reluctance oscillating motor operating under AC supply with one under DC supply. IEEE Trans Energy Convers 1999; 14(3): 328-332.

[63] Xu X, Pavlovskaia E, Wiercigroch M, Romeo F, Lenci S. Dynamic interactions between parametric pendulum and electro-dynamical shaker. ZAMM Z Angew Math Mech 2007; 87(2): 172-186.

[64] Liu Y, Pavlovskaia E, Wiercigroch M. Experimental verification of the vibro-impact capsule model. Nonlinear Dyn 2016; 83: 1029-1041.

[65] Yan Y, Liu Y, Manfredi L, Prasad S. Modelling of a vibro-impact self-propelled capsule in the small intestine. Nonlinear Dyn 2019; 96: 123-144.

[66] Guo B, Ley E, Tian J, Zhang J, Liu Y, Prasad S. Experimental and numerical studies of intestinal frictions for propulsive force optimisation of a vibro-impact capsule system, Nonlinear Dyn 2020; 101: 65-83.

[67] Cottone F, Vocca H, Gammaitoni L. Nonlinear Energy Harvesting. Phys Rev Lett 2009; 102: 080601.

[68] Wang K, Zhou J, Ouyang H, Cheng L, Xu D. A semi-active metamaterial beam with electromagnetic quasi-zero-stiffness resonators for ultralow-frequency band gap tuning. Int J Mech Sci 2020; 176(15): 105548.

[69] Foong FM, Thein CK, Yurchenko D. On mechanical damping of cantilever beam-based electromagnetic resonators. Mech Syst Signal Process 2019; 119: 120-137.

[70] Sayed M, Mousa AA, Mustafa I. Stability and bifurcation analysis of a buckled beam via active control. Appl Math Model 2020; 82: 649-665.

[71] Fleming AJ, Moheimani SOR. Inertial vibration control using a shunted electromagnetic transducer. IEEE/ASME Trans Mechatronics 2006; 11: 84-92.

[72] Yan B, Ma H, Zhang L, Zheng W, Wang K, Wu C. A bistable vibration isolator with nonlinear electromagnetic shunt damping. Mech Syst Signal Process 2020; 136: 106504.

[73] Yan B, Ma H, Yu N, Zhang L, Wu C. Theoretical modeling and experimental analysis of nonlinear electromagnetic shunt damping. J Sound Vib 2020; 471: 115184.

[74] Liu CR, Zhao R, Yu KP, Liao BP. In-plane quasi-zero-stiffness vibration isolator using magnetic interaction and cables: Theoretical and experimental study. Appl Math Model 2021; 96: 497-522.

[75] Witkowski K., Kudra G, Skurativskyi S, Wasilewski G, Awrejcewicz J. Modeling and dynamics analysis of a forced two-degree-offreedom mechanical oscillator with magnetic springs. Mech Syst Signal Process 2021; 148: 107138.

[76] Gomis-Bellmunt O, Campanile LF. Design Rules for Actuators in Active Mechanical Systems. Springer-Verlag, London; 2010.

[77] Vanderborght B, Albu-Schaeffer A, Bicchib A, et al. Variable impedance actuators: A review. Rob Auton Syst 2013; 61(12): 1601-1614 .

[78] Wiercigroch M, Kovacs S, Zhong S, Costa D, Vaziri V, Kapitaniak M, Pavlovskaia E. Versatile mass excited impact oscillator, Nonlinear Dyn 2020; 99: 323-339.

[79] Costa D, Vaziri V, Kapitaniak M, Kovacs S, Pavlovskaia E, Savi MA, Wiercigroch M. Chaos in Impact Oscillators not in Vain: Dynamics of New Mass Excited Oscillator. Nonlinear Dyn 2020; 102: 835-861.

[80] Kovacs S. Design and experimental studies of mass excited impact oscillator, PhD dissertation, University of Aberdeen, Aberdeen, UK; 2020.

[81] Keskin A. Boundary Value Problems for Engineers with MATLAB Solutions. Springer, Switzerland; 2019.

[82] Enns RH, McGuire C. Nonlinear physics with Maple for scientists and engineers. Springer, New York; 2000.

[83] Burstein L. A MATLAB Primer for Technical Programming in Materials Science and Engineering. Woodhead Publishing, Cambridge; 2020.

[84] Furlani EP. Permanent Magnet and Electromechanical Devices: Materials, Analysis, and Applications. Academic Press, London; 2001.

[85] Hao Z, Cao Q, Wiercigroch M. Nonlinear dynamics of the quasi-zero-stiffness SD oscillator based upon the local and global bifurcation analyses. Nonlinear Dyn 2017; 87: 987-1014.

[86] Zhang Z, Chen Y, Cao Q. Bifurcations and hysteresis of varying compliance vibrations in the primary parametric resonance for a ball bearing. J Sound Vib 2015; 350: 171-184.

[87] Nayfeh AH, Balachandran B. Applied Nonlinear Dynamics. Wiley-VCH, Verlag GmbH &Co. KGaA, Weinheim; 2004.

[88] Parker TS, Chua LO. Practical Numerical Algorithms for Chaotic Systems. Springer-Verlag, NewYork; 1989.